



# BULLFROG: Multi-step perturbation theory as a time integrator for cosmological simulations

Cornelius Rampf,<sup> *a,b,c,\**</sup> Florian List<sup> *b,\**</sup> and Oliver Hahn<sup> *b,c*</sup>

<sup>a</sup>Division of Theoretical Physics, Ruđer Bošković Institute, Bijenička cesta 54, 10000 Zagreb, Croatia

<sup>b</sup>Department of Astrophysics, University of Vienna, Türkenschanzstraße 17, 1180 Vienna, Austria

<sup>c</sup>Faculty of Mathematics, University of Vienna, Oskar-Morgenstern-Platz 1, 1090 Vienna, Austria

E-mail: [cornelius.stefan.rampf@irb.hr](mailto:cornelius.stefan.rampf@irb.hr), [florian.list@univie.ac.at](mailto:florian.list@univie.ac.at), [oliver.hahn@univie.ac.at](mailto:oliver.hahn@univie.ac.at)

**Abstract.** Modelling the cosmic large-scale structure can be done through numerical  $N$ -body simulations or by using perturbation theory. Here, we present an  $N$ -body approach that effectively implements a multi-step forward model based on Lagrangian Perturbation Theory (LPT) in a  $\Lambda$ CDM Universe. This is achieved by introducing the second-order accurate BULLFROG integrator, which performs 2LPT time steps (before shell-crossing) to second order without requiring the explicit computation of 2LPT displacements, while the higher-order terms rapidly approach the exact solution as the number of time steps increases. As a validation test, we compare BULLFROG against other  $N$ -body integrators and high-order LPT, both for a realistic  $\Lambda$ CDM cosmology and for simulations with a sharp UV cutoff in the initial conditions. The latter scenario enables controlled experiments against LPT and, in practice, is particularly relevant for modelling coarse-grained fluids arising in the context of effective field theory. We demonstrate that BULLFROG significantly improves upon other LPT-inspired integrators, such as FASTPM and COLA, without incurring any computational overhead compared to standard  $N$ -body integrators. Implementing BULLFROG in any existing  $N$ -body code is straightforward, particularly if FASTPM is already integrated.

**Keywords:** cosmological simulations, cosmological perturbation theory

---

\*These authors contributed equally.

---

## Contents

<b>1</b>	<b>Introduction</b>	<b>1</b>
<b>2</b>	<b>BULLFROG boiled down: a summary</b>	<b>5</b>
<b>3</b>	<b>Basic setup</b>	<b>7</b>
3.1	Perturbative treatment in Lagrangian coordinates	7
3.2	$D$ -time integrators for $N$ -body simulations	9
<b>4</b>	<b>Details of BULLFROG</b>	<b>12</b>
4.1	Initial time step	12
4.2	Arbitrary time steps	14
4.3	Numerical convergence	15
4.4	Loss of convergence through approximate growth	16
<b>5</b>	<b>Implementation and results</b>	<b>18</b>
5.1	Numerical implementation	20
5.2	Simulations with UV cutoff	21
5.3	Full $\Lambda$ CDM simulations	25
<b>6</b>	<b>Conclusions</b>	<b>28</b>
<b>A</b>	<b>KDK version of BULLFROG</b>	<b>30</b>
A.1	Determining the weights	31
A.2	Numerical convergence	32
<b>B</b>	<b>Multi-time LPT and <math>N</math>-body simulations</b>	<b>33</b>
B.1	Time-Shifted Lagrangian Perturbation Theory	35
B.2	$N$ -body force computation in light of time-shifted LPT	36

---

## 1 Introduction

Perturbation theory (PT) is an indispensable tool for interpreting cosmological observables on a wide range of spatio-temporal scales [1, 2]. In general, PT is useful whenever the underlying physics is approximately linear; prominent examples are the computation of the cosmic microwave anisotropies imprinted in the surface of last scattering [3–5], the analysis of the baryonic acoustic oscillation feature in the cosmic large-scale structure (LSS) [6–8], as well as for the general purpose of data inference of the cosmological parameters from large-scale observations [9–14].

On large cosmological scales close to the horizon, the patterns of cosmic structures are well described by linear theory as they mostly follow the overall expansion of the Universe; therefore, PT predictions are very reliable on such scales. Even on smaller scales, perturbative predictions remain fairly accurate as long as the nonlinearities are sufficiently suppressed w.r.t. to the bulk part; see e.g. refs. [15, 16] for reviews and refs. [17–24] for rather recent findings. However, standard (Eulerian) PT becomes severely hampered at smaller spatial scales, essentially due to the nonlinear accumulation of collisionless matter at focused locations, which gradually generates local density fluctuations of order unity and well beyond.

A strategy for prolonging the validity of PT – at least for some time – is to solve the underlying equations perturbatively by employing Lagrangian coordinates [25–32]. Indeed, the so-called Lagrangian Perturbation Theory (LPT) converges until trajectories of collisionless matter intersect for the first time [33–36]. This instance is called shell-crossing and is accompanied by extreme matter densities; furthermore, it implies the breakdown of conventional/standard PT [37, 38]. Recently, beyond-standard perturbative techniques have been developed, applied at the fine-grained fluid level, that allow one to go beyond shell-crossing [38–41]; however, these approaches are not mature enough to follow the halo formation process, which comes with hundreds of overlapping fluid streams.

Another way for prolonging the validity of conventional PT is to employ effective or coarse-grained fluid descriptions; see e.g. refs. [42–46]. There, one filters out small-scale density fluctuations in the initial conditions by applying suitable smoothing operations, so that the time of shell-crossing for the coarse-grained fluid is significantly extended. As a consequence, the coarse-grained fluid is still within the realm of standard PT for sufficiently strong smoothing, which, for example, enables systematic bias expansions that relate the matter dynamics to the distribution of galaxies [47]. Relating the distinct evolution of the coarse- to the fine-grained fluid is still possible, but typically requires input from numerical simulations; specifically, this input is encoded in an effective sound speed for the leading-order treatment within the effective field theory of LSS. However, from the perspective of data inference (and taking observational systematics aside), the effective description remains fully predictive on mildly nonlinear scales, even in the absence of such external inputs [48–53], provided that (1) appropriate smoothing operations are applied in the analysis of the observable at hand, and (2) that the modelling of the coarse-grained fluid is sufficiently accurate. Within a perturbative context, the last requirement implies that the smoothing needs to be sufficiently strong, although this can depend on specifics of the employed forward model (see below). At the same time, it is clear that including smaller spatial scales in the analysis would unlock more information.

In principle, drawing from the information-rich nonlinear regime of the LSS is feasible by numerical simulations. These simulations are typically implemented as  $N$ -body methods, where the continuous distribution of collisionless matter is solved by following a discrete set of  $N$  tracer particles; see ref. [16] for a recent review and an overview of related simulation techniques. The general strategy of such methods is to time-integrate the Hamiltonian equations of motion using a leapfrog/Verlet scheme, which provides asynchronous updates for the particle positions (‘drift’) and momenta (‘kick’) within a time step, consisting of three consecutive operations; these three operations are either drift-kick-drift or kick-drift-kick. Such schemes are typically second-order accurate in time, provided that the gravitational force field is sufficiently regular. Here, ‘second-order accurate’ means that at a given time, the deviation between the numerical and exact solution for the phase-space positions scales as the square of the time step.

While the drift calculation is trivial for  $N$ -body methods, the computational bottleneck relates to the kick update, as it requires evaluating the current gravitational force field, which is subject to solving the cosmological Poisson equation. The computational complexity for the kick update is typically  $O(N \log N)$  [16], and thus is sensitive to the number of tracer particles. Unfortunately, to cover the vast range of scales of current and upcoming galaxy and radio surveys [54–58], very expensive simulations are required [59–62], involving  $10^{12} - 10^{13}$  and more tracer particles. Even worse, a statistical analysis for retrieving the unknown cosmological parameters requires not just one, but a large set of expensive simulations (although machine-learning techniques, or the use of differentiable simulations could greatly reduce this complexity [63–67]). Therefore, when leveraging cosmological simulations for the purpose of parameter inference, it is crucial to minimise their computational costs.

One way to improve the efficiency of an  $N$ -body simulation is the development of fast time-integration methods [68–73] (see e.g. refs. [74–79] for other fast simulation/hybrid techniques). There,

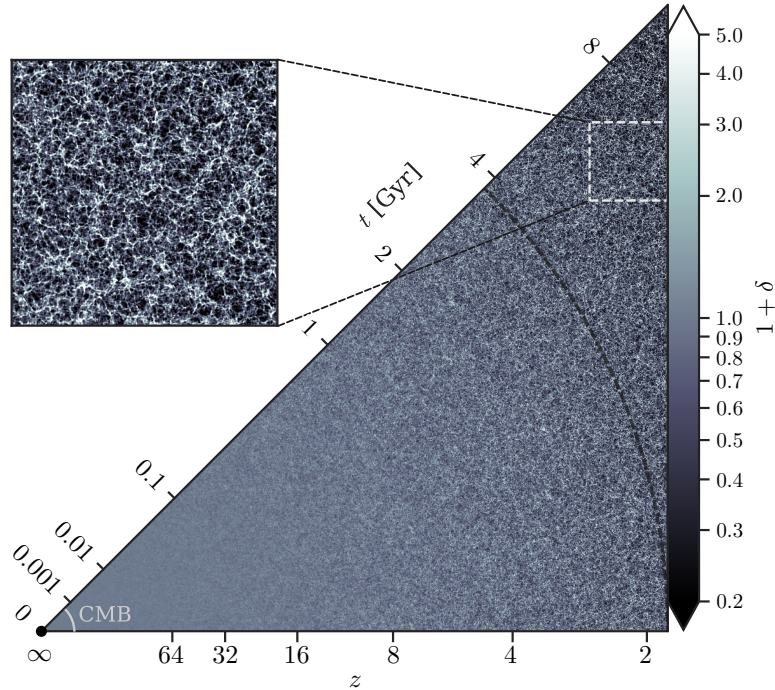


**Figure 1.** Light cone of cosmic structures as seen by photons propagating from the Big Bang until today, obtained by exploiting our unified framework. Here,  $1 + \delta$  denotes the matter overdensity.

the time integrator of the simulation is fine-tuned to incorporate analytical knowledge of cosmic structure formation, which is (currently) provided by PT (the sky is the limit), implying that only few (i.e. 10 – 100) time steps are required to accurately reproduce the statistics on mildly nonlinear scales. Obviously, ‘less time steps’ imply ‘less force calculations,’ and thus, fast methods have the potential to alleviate the core bottleneck of numerical simulations.

An important example of a fast time-integrating method is FASTPM [70], which, to the leading order, comes with built-in Zel’dovich motion a.k.a. first-order LPT, where the latter comprises the bulk part of the evolution of collisionless matter on very large scales. This integrator is second-order accurate and symplectic, as recently analysed in ref. [72]. In fact, FASTPM belongs to a class of cosmological integrators [72], all of which can be made consistent with Zel’dovich motion to the leading order. The essence of such *D-time integrators* is that the momentum is not canonically related to the position of particles, but instead defined by the rate of change of particle positions with respect to the growth time  $D = D_+$  of linear density fluctuations in a  $\Lambda$ CDM Universe. Amongst others, ref. [72] introduced POWERFROG, which is their most powerful *D-time* integrator in terms of computational performance and efficiency. Unlike FASTPM, this integrator accurately matches second-order LPT for sufficiently early times. This capability allows us to start *N*-body simulations at time zero and analyse the emergence of cosmic structures within a unified framework (i.e., without switching from LPT to *N*-body at some intermediate time as commonly done); see figure 1.

In this paper, we introduce BULLFROG, short for Blazingly fast UV-complete LPT-informed LeapFROG, which is a *D-time* integrator as well. BULLFROG is the first integrator that, to second order, is in accordance with second-order LPT in  $\Lambda$ CDM after each completed time step (which POWERFROG achieved only for the initial step starting at  $D = 0$ ). In essence, BULLFROG implements a multi-time-stepping variant of 2LPT, where the latter is, in fact, a single time-step approach (since the LPT displacement is the result of integrating the fluid equations from initial to final time). Even

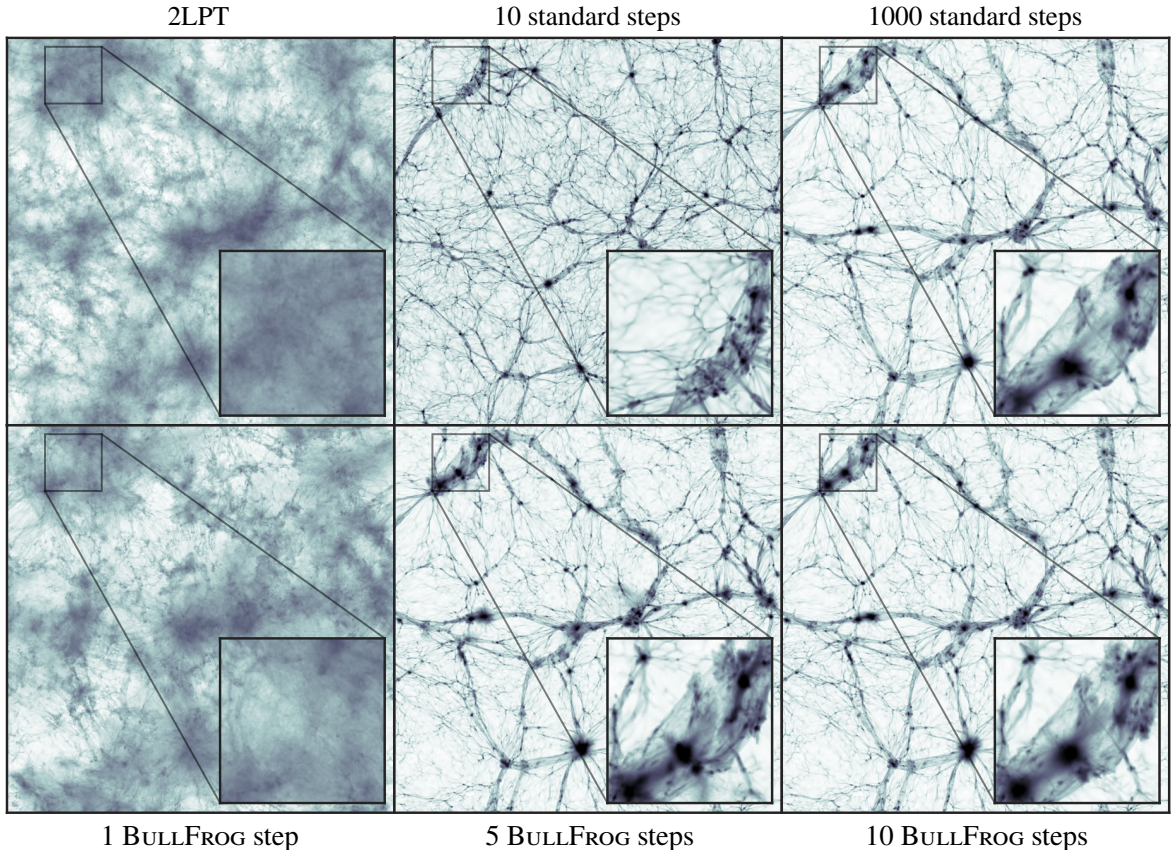


**Figure 2.** Razor-thin slices through today’s overdensity field obtained using various forward models for a  $(25 h^{-1} \text{ Mpc})^3$  box containing  $512^3$  particles (see section 5 for implementation details and quantitative results). Simulations with ‘standard steps’ were conducted using a standard symplectic leapfrog integrator, initialised at  $z = 127$  with 2LPT. While 10 standard steps lead to the formation of small-scale structure, the growth of large-scale structure deviates significantly from the reference simulation, which was obtained with 1000 standard steps. By contrast, BULLFROG already performs slightly better than 2LPT for a single step, and converges rapidly across all scales as the number of steps increases.

more, building 2LPT into BULLFROG enables high accuracy, far beyond the 2LPT level, even with a limited number of time steps; see figure 2 for a demonstration.

From the perspective of LPT, one can explain the performance gain of BULLFROG as follows: Standard LPT takes as input the initial gravitational field, and seeks power-series solutions around a unique temporal expansion point (usually about  $D = 0$ ). By contrast, BULLFROG receives consecutive 2LPT updates on the evolved gravitational field during each kick calculation and thus has a significant advantage over single-step LPT, which basically needs to forecast the evolution of the gravitational field based on the initial conditions. In many respects, BULLFROG could be viewed as a near-optimal (and easy to access!) implementation of LPT, as arbitrarily accurate-in-time solutions are achieved, simply by executing as many time steps as needed to reach a certain target accuracy. Alternatively, one could use ‘single-time-step’ LPT to (much) higher orders to achieve comparable accuracy, at least until shell-crossing; however, as it turns out, generating  $n$ LPT solutions with  $n \gtrsim 4$  is in general not recommended, mainly due to a sweeping memory footprint at high orders, needed to store and de-alias the (longitudinal and transverse) perturbation fields [35, 80]. By contrast, BULLFROG is UV-complete in the temporal sense – even after shell-crossing – and is basically only limited by the number of force

computations. For future applications, we envision BULLFROG not only to be used as a standalone technique for rapid LSS modelling, but also as a valuable tool in the development of hybrid methods, such as within the framework of effective field theory where BULLFROG could replace the commonly used perturbative forward model.

This paper is organised as follows. In section 2, we outline the essence of BULLFROG. Sections 3 and 4 respectively introduce the basic framework and provide more details on BULLFROG. Experienced readers interested only in the results may skip directly to section 5. We conclude in section 6.

*Notation:* We employ comoving Eulerian coordinates  $\mathbf{x} = \mathbf{r}/a$ , where  $\mathbf{r}$  are physical coordinates, and  $a$  is the cosmic scale factor, normalised to unity at the present time. Lagrangian coordinates are dubbed  $\mathbf{q}$ . We use  $\nabla_{\mathbf{q}}$  and  $\nabla_{\mathbf{q}}^{-2}$  to denote respectively the partial derivative and inverse Laplacian w.r.t.  $\mathbf{q}$ , and we define  $\nabla_{\mathbf{q}}^{-1} := \nabla_{\mathbf{q}}^{-2} \nabla_{\mathbf{q}}$ . Partial derivatives w.r.t. the spatial component  $q_i$  are abbreviated with  $g_{,i} := \nabla_{q_i} g$ . We employ the unnormalised  $\Lambda$ CDM linear growth function  $D(a) = a {}_2F_1(1/3, 1, 11/6; -\Lambda a^3) = a - (2\Lambda/11)a^4 + O(a^7)$  as a temporal variable (represented by the Gauss hypergeometric function), where  $\Lambda = \Omega_{\Lambda 0}/\Omega_{m 0}$  is the ratio of the present-day values of the dark-energy and matter densities.  $D$ -time derivatives are denoted with  $T' := \partial_D T$  for any given time-dependent function  $T = T(D)$ . Temporal advancements from  $D : D_n \rightarrow D_{n+1}$  are linked to the (potentially nonuniform) increment  $\Delta D := D_{n+1} - D_n > 0$  from step  $n$  to  $n + 1$ , where we omit the index ‘ $n$ ’ on  $\Delta D$  to avoid cluttering. Temporal evaluations w.r.t. to step  $n$  are abbreviated with  $T_n := T|_{D=D_n}$ .

*Nomenclature:* We call an integrator ‘ZA consistent’ or ‘2LPT consistent,’ if its particle trajectories and momenta agree respectively with the predictions of first- or second-order Lagrangian perturbation theory after each completed time step, up to higher-order terms, and before shell-crossing. The integrators BULLFROG, POWERFROG and FASTPM are frequently abbreviated with BF, PF, and FPM, respectively. Performing  $n$  linear-in- $D$  steps with BULLFROG is denoted with  $n$ BF, and similarly for the other  $D$ -time integrators. For COLA,  $n$  linear-in- $a$  steps are dubbed  $n$ COLA.

## 2 BULLFROG boiled down: a summary

We employ the linear  $\Lambda$ CDM growth function  $D = a + O(\Lambda a^4) = D_n$  as a time variable, where  $n$  is a step counter linked to the temporal advancement of the system with (potentially non-uniform) increment  $\Delta D = D_{n+1} - D_n > 0$ . Considering a drift-kick-drift (DKD) scheme from step  $n \rightarrow n + 1$  with intermediate updates provided at  $D_{n+1/2} = D_n + \Delta D/2$ , BULLFROG determines (dropping  $N$ -particle indices for simplicity)

$$\mathbf{x}_{n+1/2} = \mathbf{x}_n + \frac{\Delta D}{2} \mathbf{v}_n, \quad \text{D} \quad (2.1a)$$

$$\mathbf{v}_{n+1} = \alpha \mathbf{v}_n + \beta D_{n+1/2}^{-1} \mathbf{A}(\mathbf{x}_{n+1/2}), \quad \text{K} \quad (2.1b)$$

$$\mathbf{x}_{n+1} = \mathbf{x}_{n+1/2} + \frac{\Delta D}{2} \mathbf{v}_{n+1}. \quad \text{D} \quad (2.1c)$$

Here,  $\mathbf{x}_n$  and  $\mathbf{v}_n = \partial_D \mathbf{x}_n$  denote respectively fluid-particle positions and velocity evaluated at step  $n$ , while  $\mathbf{A}$  is the gravitational field, associated to the Poisson equation  $\nabla_{\mathbf{x}} \cdot \mathbf{A} = -\delta$ , where  $\delta = \rho/\bar{\rho} - 1$  is the density contrast. Furthermore,  $(\alpha, \beta)(D_n, \Delta D)$  are temporal weights that, for BULLFROG, are fixed by a 2LPT matching condition, a procedure that is briefly outlined below; see eq. (2.3) for the results of  $(\alpha, \beta)$ .

Since the leapfrog integrator approximates the continuous particle trajectories in a piecewise linear manner, the positions of the  $N$ -body particles after the first half drift (2.1a) will, in general, not agree with the exact solution (blue dotted curve in figure 3). As a consequence, for finite time

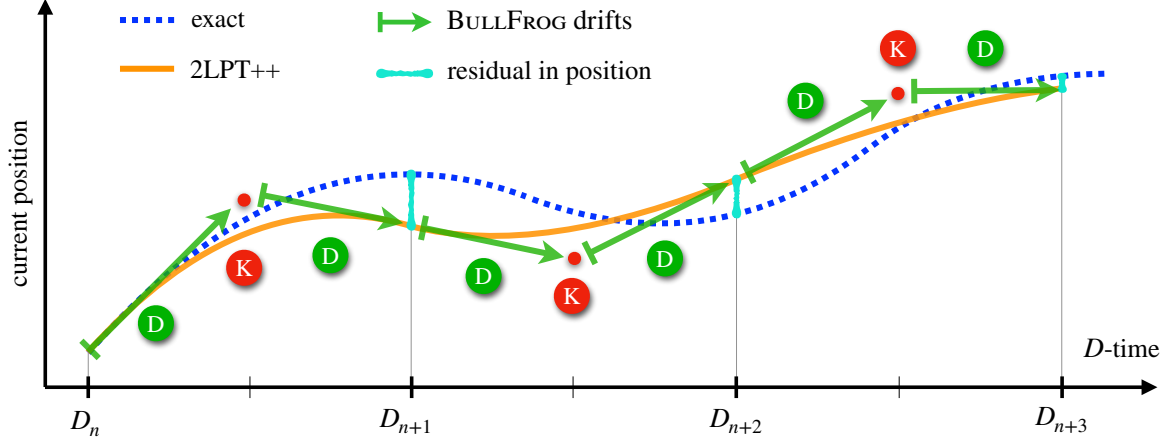


**Figure 3.** Sketch of temporal integrator operations built into BULLFROG (shown as green arrows and red dots, labelled with ‘D’ for drift and ‘K’ for kick), compared against the exact solution which is achieved by  $\infty$ LPT before shell-crossing (blue dotted curve). Due to temporal discretisation, the  $N$ -body integrator evaluates the force field at a slightly misplaced position after each first half drift (red dots) relative to the exact position. BULLFROG takes the force field from this position as input and adjusts the temporal weights ( $\alpha, \beta$ ) during the kick operation, such that the truncated 2LPT trajectory is exactly recovered after each completed time step (notably without explicitly computing the spatial 2LPT kernel). On top of that, an infinite tower of higher-order terms is excited during the force calculation; therefore, we call the resulting trajectory 2LPT++ (orange curve). BULLFROG receives a refined update on the evolving gravitational field at each step, and its trajectory converges to the exact solution as the step size decreases – even after shell-crossing. BULLFROG can be initialised directly at time zero, i.e., without the use of (external) initial-condition generators.

step size, the force field during the kick operation is determined at a misplaced position (red dots in figure 3), in the following dubbed  $\mathbf{x}_{\text{mis}}$ . To correct for this misplacement, we exploit Einstein’s weak equivalence principle, and compute the gravitational field along the particle accelerations of the misplaced trajectories,

$$(\nabla_{\mathbf{x}} \cdot \mathbf{A})|_{\mathbf{x}=\mathbf{x}_{\text{mis}}} = -\delta(\mathbf{x}_{\text{mis}}). \quad (2.2)$$

Here, the nonlinear density contrast  $\delta(\mathbf{x}_{\text{mis}})$  is evaluated at the time of the half step. Straightforward calculations (in Lagrangian coordinates) then allow us to determine  $\mathbf{A}$  by perturbative means. Crucially, the computation of  $\mathbf{A}$  generates an infinite tower of nonlinear terms, regardless of the level of (perturbative) approximation inherent in the misplaced trajectories. Considering then the *leading nonlinear correction* in  $\mathbf{A}$  allows us to determine the weights ( $\alpha, \beta$ ), so that the drift and kick updates are 2LPT consistent after each completed time step at  $D_{n+1}$  for any  $n \geq 0$ , up to higher-order effects and before shell-crossing. In summary, we find for the two weights of the BULLFROG integrator the following expressions

$$\alpha = \frac{E'_{n+1} - F_{n+1/2}}{E'_n - F_{n+1/2}} \stackrel{\text{EdS}}{\asymp} \frac{4\mathfrak{n}(4\mathfrak{n} + 1) - 5}{4\mathfrak{n}(4\mathfrak{n} + 7) + 7}, \quad \beta = 1 - \alpha \stackrel{\text{EdS}}{\asymp} \frac{24\mathfrak{n} + 12}{4\mathfrak{n}(4\mathfrak{n} + 7) + 7}, \quad (2.3)$$

where  $E'_n = \partial_D E|_{D=D_n}$ , ‘EdS’ refers to the Einstein–de Sitter cosmological model ( $\Omega_{\text{m}0} = 1$ ), and we have defined  $\mathfrak{n} := a_n/\Delta a$  (which is equal to  $n$  for uniform time stepping). Furthermore,  $E$  is the second-order growth function of the LPT displacement in  $\Lambda$ CDM [29, 81], and

$$F_{n+1/2} := D_{n+1/2}^{-1} \left( E_n + E'_n \frac{\Delta D}{2} \right) - D_{n+1/2}. \quad (2.4)$$

Calculating the weights in  $\Lambda$ CDM involves the numerical integration of ordinary differential equations for  $D$  and  $E$  (see eqs. 3.5); besides that, no further computational overhead is required for BULLFROG compared to standard  $N$ -body integrators. See appendix A for the KDK version of BULLFROG.

Readers not interested in the basics and technical details can go directly to the results section 5.

### 3 Basic setup

Before delving into the details of our approach, let us begin by building up the basic framework. A host of numerical and theoretical approaches for the LSS aim to solve the cosmological Vlasov–Poisson system, which encodes the evolution of the distribution  $f(\mathbf{x}, \mathbf{p}, t)$  of collisionless matter, i.e.,

$$\frac{df}{dt} = \frac{\partial f}{\partial t} + \frac{\mathbf{p}}{a^2} \cdot \nabla_{\mathbf{x}} f - \nabla_{\mathbf{x}} \phi \cdot \nabla_{\mathbf{p}} f = 0, \quad \nabla_{\mathbf{x}}^2 \phi = 4\pi G \bar{\rho} a^2 \delta. \quad (3.1)$$

Here,  $\mathbf{x} = \mathbf{r}/a$  denote comoving coordinates composed of physical coordinates  $\mathbf{r}$  and cosmic scale factor  $a$  for a  $\Lambda$ CDM Universe,  $\mathbf{p}$  is the momentum variable canonically conjugated to  $\mathbf{x}$ , and the density contrast  $\delta = (\rho - \bar{\rho})/\bar{\rho}$  is defined through

$$\rho(\mathbf{x}, t) = \bar{\rho}(t) [1 + \delta(\mathbf{x}, t)] = \int f(\mathbf{x}, \mathbf{p}, t) d^3 p, \quad (3.2)$$

where  $\bar{\rho}(t) \propto a^{-3}$  is the background density. In this paper we focus on two distinct basic frameworks to solve eq. (3.1), namely by perturbative means valid before shell-crossing (section 3.1), and  $N$ -body methods based on  $D$ -time integrators (section 3.2), both of which we briefly describe in the following.

#### 3.1 Perturbative treatment in Lagrangian coordinates

**Standard Lagrangian perturbation theory.** For cold initial conditions, it is convenient to formulate eqs. (3.1) in Lagrangian space, where the initial/Lagrangian coordinates  $\mathbf{q}$  serve as fluid labels for the matter elements that evolve to their current positions  $\mathbf{x}(\mathbf{q}, t)$ . Denoting with an overdot the total time derivative w.r.t. time  $t$ , the Lagrangian evolution equations in  $\Lambda$ CDM are

$$\ddot{\mathbf{x}} + 2H\dot{\mathbf{x}} = -a^{-2}\nabla_{\mathbf{x}}\phi, \quad \nabla_{\mathbf{x}}^2\phi = 4\pi G\bar{\rho}a^2\delta, \quad (3.3)$$

where  $(H/H_0)^2 = \Omega_{m0}a^{-3} + \Omega_{\Lambda0}$  and, in Lagrangian coordinates and until shell-crossing, the density contrast is expressed by the Jacobian determinant  $J(\mathbf{x}(\mathbf{q}, t)) = \det[\nabla_{\mathbf{q}}\mathbf{x}]$ ,

$$\delta(\mathbf{x}(\mathbf{q}, t)) + 1 = J^{-1}(\mathbf{x}(\mathbf{q}, t)). \quad (3.4)$$

In LPT, these equations are solved by a perturbative expansion of the displacement field  $\boldsymbol{\psi} = \mathbf{x} - \mathbf{q}$ ; here we just state the well-known results up to second order and refer the reader to e.g. refs. [15, 16, 25, 26, 30–32] for details and reviews. Expanding the displacement up to first order in a small parameter  $\epsilon > 0$  and keeping only linear terms in  $\epsilon$  in the equations of motion, one arrives at the well-known Zel’dovich approximation (ZA)

$$\mathbf{x}^{\text{ZA}} := \mathbf{q} + \boldsymbol{\psi}^{\text{ZA}}, \quad \boldsymbol{\psi}^{\text{ZA}} := \boldsymbol{\psi}^{(1)} = -D\nabla_{\mathbf{q}}\varphi^{\text{ini}}, \quad \text{with } \ddot{D} + 2H\dot{D} = 4\pi G\bar{\rho}D. \quad (3.5a)$$

Here,  $D = a - (2\Lambda/11)a^4 + O(a^7\Lambda^2)$  is the  $\Lambda$ CDM growing-mode solution and  $\Lambda = \Omega_{\Lambda0}/\Omega_{m0}$ , while

$$\varphi^{\text{ini}}(\mathbf{q}) := D^{-1}(a_{\text{today}}) \nabla_{\mathbf{q}}^{-2} \delta_{\text{lin}}(\mathbf{q}, a_{\text{today}}) \quad (3.5b)$$



is the gravitational potential backscalded to ‘initial time’  $D = 0$ , expressed by today’s linear matter density contrast, retrieved from standard Einstein–Boltzmann solvers.<sup>1</sup> Here and in the following, we initialise the fluid at time  $D = 0$  in the growing mode, which is well defined provided one imposes the initial conditions  $\delta(D = 0) = 0$  and  $(\partial_D \mathbf{x})|_{D=0} = -\nabla_{\mathbf{q}} \varphi^{\text{ini}}$ ; see e.g. ref. [82, 83] for details.

Likewise, expanding the displacement to second order, one finds the well-known 2LPT solution

$$\mathbf{x}^{2\text{LPT}} := \mathbf{q} + \boldsymbol{\psi}^{2\text{LPT}}, \quad \boldsymbol{\psi}^{2\text{LPT}} := \boldsymbol{\psi}^{(1)} + \boldsymbol{\psi}^{(2)}, \quad (3.5c)$$

where

$$\boldsymbol{\psi}^{(2)} = E \nabla_{\mathbf{q}}^{-1} \mu_2, \quad \text{with } \ddot{E} + 2H\dot{E} = 4\pi G \bar{\rho} (E - D^2). \quad (3.5d)$$

Here,  $\nabla_{\mathbf{q}}^{-1} := \nabla_{\mathbf{q}}^{-2} \nabla_{\mathbf{q}}$ , and  $\mu_2 = (1/2)[\varphi_{,ll}^{\text{ini}} \varphi_{,mm}^{\text{ini}} - \varphi_{,lm}^{\text{ini}} \varphi_{,lm}^{\text{ini}}]$  is a purely spatial kernel (summation over repeated indices is assumed), while  $E = -(3/7)D^2 - (3\Lambda/1001)D^5 + O(\Lambda^2 D^8)$  is the fastest growing-mode solution at second order in  $\Lambda\text{CDM}$  (which can also be expressed in terms of hypergeometric functions, see ref. [81, eq. 22]). Note that for BULLFROG we do *not* employ the ‘ $D^n$  approximation’  $E \simeq -(3/7)D^2$  which would ignore explicit  $O(\Lambda)$  corrections, nor do we employ the refined approximation of ref. [29], as both would spoil the convergence of the proposed integrator; see section 4.4 for details.

Since the ZA solution (3.5a) is proportional to  $D$ , it turns out to be convenient – in LPT but also for the proposed integrator – to define a suitably rescaled velocity

$$\mathbf{v} = \partial_D \mathbf{x} \quad (3.6)$$

such that, to the leading order, the rescaled velocity is constant in the  $D$ -time before shell-crossing. Here,  $\partial_D$  is the Lagrangian  $D$ -time derivative, and the ZA and 2LPT velocities read respectively

$$\mathbf{v}^{\text{ZA}} = -\nabla_{\mathbf{q}} \varphi^{\text{ini}}, \quad \mathbf{v}^{2\text{LPT}} = \partial_D \boldsymbol{\psi}^{2\text{LPT}} = -\nabla_{\mathbf{q}} \varphi^{\text{ini}} + \partial_D E \nabla_{\mathbf{q}}^{-1} \mu_2. \quad (3.7)$$

**Particle acceleration along approximate trajectories.** As a somewhat non-standard exercise, we will need an expression for the gravitational field  $\mathbf{A}$ , self-induced by the advected particles,

$$\boxed{\mathbf{A} := -\nabla_{\mathbf{x}} \varphi, \quad \nabla_{\mathbf{x}}^2 \varphi := \delta}, \quad (3.8)$$

where we have rescaled the cosmological potential according to

$$\varphi = \frac{\phi}{4\pi G \bar{\rho} a^2}. \quad (3.9)$$

The quantity  $\mathbf{A}$  and its perturbative treatment play a central role in this paper. In particular, we need to determine  $\mathbf{A}$  along approximate trajectories, which could be based on ZA or 2LPT motion (or anything else). Crucially and distinct to standard LPT, however, the approximate trajectories are taken as input and are not perturbatively refined, while the resulting gravitational acceleration is truncated to arbitrary order (here: to second order). To demonstrate how  $\mathbf{A}$  can be solved along a given (approximate) trajectory, let us determine it for the case when  $\mathbf{x} = \mathbf{x}^{\text{ZA}}$ , for which we consider

$$(\nabla_{\mathbf{x}} \cdot \mathbf{A})|_{\mathbf{x}=\mathbf{x}^{\text{ZA}}} = -\delta(\mathbf{x}^{\text{ZA}}). \quad (3.10)$$

<sup>1</sup>We normalise today’s scale factor to unity, but work, unless stated otherwise, with the ‘unnormalised’ growth  $D = a + O(\Lambda a^4)$ , which is in particular relevant when implementing BULLFROG. In this context, while the *normalised* growth function  $D/D(a_{\text{today}})$  could also be used as a time variable, normalising the second-order growth function  $E$  involves  $D(a_{\text{today}})$  quadratically, requiring manual reversion of this normalisation when computing the kick coefficients.

To proceed, we convert the Eulerian derivative into Lagrangian ones, using  $\nabla_{x_i} = (\nabla_{x_i} q_j) \nabla_{q_j}$ , where  $\nabla_{x_i} q_j = \varepsilon_{ikl} \varepsilon_{jmn} x_{k,m} x_{l,n} / (2J)$ , and  $\varepsilon_{ikl}$  is the Levi-Civita symbol. Straightforward derivations then lead to

$$\left[ (1 - D\varphi_{,ll}^{\text{ini}}) \delta_{ij} + D\varphi_{,ij}^{\text{ini}} + h.o.t. \right] A_{i,j}^{\text{ZA}} = J_{\text{ZA}} - 1, \quad (3.11)$$

where  $J_{\text{ZA}} = 1 - D\varphi_{,ll}^{\text{ini}} + D^2\mu_2 + h.o.t.$ . Here and in the following, ‘*h.o.t.*’ stands for higher-order terms. We solve this equation by a standard perturbative Ansatz  $A^{\text{ZA}} := A^{(1)}\epsilon + A^{(2)}\epsilon^2 + \dots$ , yielding

$$A^{\text{ZA}} = -D\nabla_{\mathbf{q}}\varphi^{\text{ini}} - D^2\nabla_{\mathbf{q}}^{-1}\mu_2 + h.o.t. \stackrel{\text{EdS}}{\approx} -a\nabla_{\mathbf{q}}\varphi^{\text{ini}} - a^2\nabla_{\mathbf{q}}^{-1}\mu_2 + h.o.t. \quad (3.12)$$

Likewise, we can determine the acceleration along 2LPT trajectories, for which we need  $J_{2\text{LPT}} = 1 - D\varphi_{,ll}^{\text{ini}} + (E + D^2)\mu_2 + h.o.t.$  as updated input, leading to

$$A^{2\text{LPT}} = -D\nabla_{\mathbf{q}}\varphi^{\text{ini}} + (E - D^2)\nabla_{\mathbf{q}}^{-1}\mu_2 + h.o.t. \stackrel{\text{EdS}}{\approx} -a\nabla_{\mathbf{q}}\varphi^{\text{ini}} - \frac{10}{7}a^2\nabla_{\mathbf{q}}^{-1}\mu_2 + h.o.t., \quad (3.13)$$

where, notably, the second-order term has an altered temporal coefficient in comparison to the ZA acceleration (3.12), due to the 2LPT contribution in the Jacobian. Here it is important to observe that, no matter whether the trajectories are approximated with ZA or with higher-order schemes, the associated gravitational acceleration always contains an infinite number of perturbative terms (except in the one-dimensional case). This point is in particular crucial for  $N$ -body integrators where a fairly similar hierarchy of nonlinear terms is generated when determining the  $N$ -body forces (see section 4).

Finally, for future reference, we remark that beyond second order, there will be transverse contributions to  $\mathbf{A}$ , virtually for the same reason as observed in standard LPT [84, 85]. To get the governing equation, we multiply the definition  $A_l = -\nabla_{x_l}\varphi$  by the matrix with elements  $\partial x_l / \partial q_j$ , leading firstly to  $x_{l,j} A_l = -\nabla_{q_j}\varphi$ . Taking from this the Lagrangian curl  $\varepsilon_{ijk}\partial_{q_k}$ , we arrive at

$$\varepsilon_{ijk} x_{l,j} A_{l,k} = 0, \quad (3.14)$$

which is a vector equation that is related to the so-called Cauchy invariants (see e.g. [32] for details and historical context). Of course, eqs. (3.14) can also be evaluated along approximate trajectories.

### 3.2 $D$ -time integrators for $N$ -body simulations

Standard  $N$ -body methods employ tracer particles that follow the evolution of the continuous phase-space distribution  $f(\mathbf{x}, \mathbf{p}, t)$ ; see, e.g., refs. [16, 86, 87] for reviews. This is effectively implemented by replacing the functional dependencies of the distribution function from  $(\mathbf{x}, \mathbf{p})$  to  $(\mathbf{x}_i, \mathbf{p}_i)$ , where  $i = 1, \dots, N$  denote the  $N$  particle labels; but note that, here and in the following, we will omit the particle labels to avoid unnecessary cluttering. The ‘discretised’ formulation of Vlasov–Poisson relies on the associated Hamiltonian equations of motion  $\partial_t \mathbf{x} = \mathbf{p}/a^2$  and  $\partial_t \mathbf{p} = -\nabla_{\mathbf{x}}\phi$  with  $\nabla_{\mathbf{x}}^2\phi = 4\pi G\bar{\rho}a^2\delta$ , where all expressions – including the density – are evaluated along  $N$  fluid characteristics. Importantly, the continuous potential  $\phi$  in the Poisson equation is approximated by the discrete potential sourced by the tracer particles. In this work, we will assume that the spatial resolution and the accuracy of the force computation are sufficient to adequately represent the underlying continuous dynamics, and focus on the *temporal* discretisation of Vlasov–Poisson. In practice, this necessitates the use of ‘discreteness-reduction techniques’ at early times, see e.g. refs. [73, 83, 88, 89] for related avenues.

Typically, the Hamiltonian equations are time integrated using symplectic leapfrog schemes, as for example executed with consecutive kick-drift-kick operations, implemented in widely employed codes such as GADGET, PKDGRAV-3, RAMSES, and SWIFT [90–93]. Symplectic leapfrog schemes

employ canonically conjugate variables in their drift and kick updates, providing certain stability properties for energy-preserving systems. On cosmological scales, however, energy is continuously extracted from the Vlasov–Poisson system due to the presence of the Hubble drag term in comoving coordinates. As a result, the benefit of enforcing symplecticity on cosmological scales is questionable, although it is relevant for simulating virialised systems that have decoupled from the Hubble flow.

Here we follow a different strategy and work with ‘ $D$ -time integrators’ (called  $\mathcal{H}$  integrators in refs. [72, 73]), which are closely related to the basic setup of LPT. Indeed, with  $D$ -time integrators, one works with the phase-space variables  $(\mathbf{x}, \mathbf{v})$  where, importantly,  $\mathbf{v} := \partial_D \mathbf{x}$ , which is *not* the canonical conjugate to  $\mathbf{x}$ . Employing  $D$ -time integrators, a generic drift-kick-drift advancement from  $D : D_n \rightarrow D_{n+1}$  is performed according to [72]

$$\mathbf{x}_{n+1/2} = \mathbf{x}_n + \frac{\Delta D}{2} \mathbf{v}_n, \quad (3.15a)$$

$$\mathbf{v}_{n+1} = \alpha \mathbf{v}_n + \beta D_{n+1/2}^{-1} \mathbf{A}(\mathbf{x}_{n+1/2}), \quad (3.15b)$$

$$\mathbf{x}_{n+1} = \mathbf{x}_{n+1/2} + \frac{\Delta D}{2} \mathbf{v}_{n+1}, \quad (3.15c)$$

where  $\alpha$  and  $\beta$  are temporal weights that can be chosen such that the integrator has certain properties (most importantly convergence towards the correct solution as  $\Delta D \rightarrow 0$ ).

An important example of a  $D$ -time integrator is FASTPM [70–72], which is ZA consistent after each completed time step (achieved by requiring  $\alpha + \beta = 1$ ), is symplectic and second-order accurate. The weights for the DKD version of FASTPM (FPM) are [72]

$$\alpha^{\text{FPM}} = \frac{\mathcal{F}_n}{\mathcal{F}_{n+1}}, \quad \beta^{\text{FPM}} = 1 - \alpha^{\text{FPM}}, \quad (3.16)$$

with

$$\mathcal{F}(a) := a^3 H \partial_a D, \quad \mathcal{F}_n := \mathcal{F}(a(D))|_{D=D_n}, \quad (3.17)$$

where  $a(D)$  is the inverse of  $D(a)$ ; in passing, we note that  $\mathcal{F}$  is defined by  $\mathbf{p} = a^2 \partial_t \mathbf{x} = \mathcal{F} \partial_D \mathbf{x}$ . Differentiable implementations of FASTPM, such as FLOWPM [65] and PMWD [66], also exist and can be conveniently interfaced with inference and sampling methods that rely on gradient information, such as Hamiltonian Monte Carlo. We remark that in this paper we only consider the DKD version of FASTPM, and for consistency we perform linear-in- $D$  steps also with FASTPM (whereas the original implementation uses linear-in- $a$  steps).

In addition to FASTPM, we will also compare our predictions against POWERFROG (PF) recently introduced in ref. [72], which is also a  $D$ -time integrator and comes with the weights

$$\alpha^{\text{PF}} = \begin{cases} -5/7; & n = 0, \\ \left( c_1 D_n^{c_2} + c_3 D_{n+1}^{c_2} \right) D_{n+1/2}^{-c_2} + c_4; & n > 0, \end{cases}, \quad \beta^{\text{PF}} = 1 - \alpha^{\text{PF}}. \quad (3.18)$$

Here, the numerical coefficients  $c_1 - c_4$  result from solving a transcendental system of equations (see ref. [72] for details); once the weights are fixed, the POWERFROG integrator is second-order accurate and in general ZA consistent and additionally 2LPT consistent for the first step at  $D = 0$ . We remark that POWERFROG approximates the second-order growth effectively with  $E \simeq -(3/7)D^2$  during the first time step, which however is only accurate at sufficiently early times when the impact of the cosmological constant on the matter dynamics is still negligible ( $z \gtrsim 10$ ). We will shortly see that BULLFROG rectifies these shortcomings.

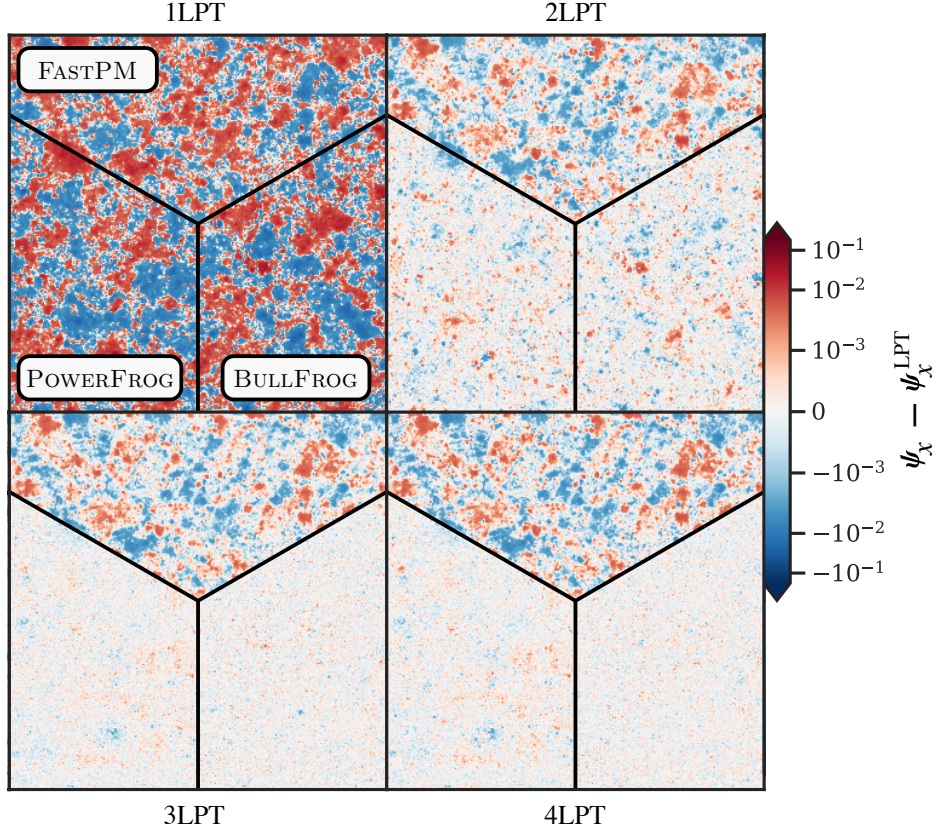


**Figure 4.** Residuals of the first displacement component  $\psi_x$  between the  $D$ -time integrators for the threefold step  $z : \infty \rightarrow 50 \rightarrow 24 \rightarrow 16$  and  $n$ LPT in a single time step for the orders  $n = 1 - 4$ . Shown is a razor-thin slice in the Lagrangian  $y$ - $z$  plane with a side length of  $300 \text{ Mpc}/h$ , using  $N = 512^3$  particles. Here, all particles are still in the single-stream regime, for which LPT converges towards the exact solution.

All  $D$ -time integrators have in common that the corresponding simulations can be directly initialised at  $D = D_0 = 0$  (the Big Bang), specifically by employing the initial conditions

$$D_0 : \quad \mathbf{x}_0 = \mathbf{q}, \quad \mathbf{v}_0 = -\nabla_{\mathbf{q}} \varphi^{\text{ini}}, \quad (3.19)$$

which correspond to growing-mode initial conditions as employed in LPT (see section 3.1). Indeed, the first statement in eqs. (3.19) implies an initially vanishing density contrast, while the second condition implies ZA motion in the continuous limit. In the literature, these so-called ‘slaved’ initial conditions play a central role in generating initial displacements in standard  $N$ -body simulations [17, 83, 94, 95], and comprise the foundation of demonstrations of LPT convergence [33–35].

Figure 4 shows a performance test of the three  $D$ -time integrators, conducted at the field level and evaluated at sufficiently high redshifts, where LPT remains very accurate (see section 5 for details on the numerical implementation and for late-time results). Specifically, we show the difference in the displacement component  $\psi_x$  between the  $D$ -time integrators for the three-step sequence  $z : \infty \rightarrow 24 \rightarrow 20 \rightarrow 16$  and  $n$ LPT in a single time step for the orders  $n = 1 - 4$ . It is seen that the residuals for both BULLFROG and POWERFROG with respect to 3 – 4LPT are very small, already with as few as three time steps. As expected, the performance is slightly better for BULLFROG than for POWERFROG due to the built-in 2LPT matching conditions of the former at each time step, which the latter achieves only for the first time step. Thus, with BULLFROG, only  $n$ LPT residuals

with  $n \geq 3$  remain – which become increasingly smaller as the step size is reduced. By contrast, the residuals of FASTPM against high-order LPT are clearly populated by a 2LPT contribution, since FASTPM only incorporates ZA motion for each time step. In summary, figure 4 demonstrates that BULLFROG achieves the best agreement with the high-order LPT solution for a given number of time steps in comparison with the other  $D$ -time integrators.

## 4 Details of BULLFROG

Here, we provide details about the new integrator BULLFROG, which comes with the unique choice of weights  $(\alpha, \beta)$  within the class of  $D$ -time integrators that is 2LPT consistent after each completed time step. For pedagogical reasons, we first discuss the initial step in section 4.1, while we provide derivations valid for any time step in section 4.2. In section 4.3, we show that this 2LPT-consistent choice of the weights defines a second-order accurate integrator, and section 4.4 addresses the loss of convergence if approximate displacement growth is used. In the present section we only consider the DKD form; see appendix A for the KDK version of BULLFROG.

The general strategy is as follows (see also figure 3). Due to temporal discretisation, the gravitational force during the kick step is in general not identical to that evaluated on the 2LPT trajectory (cf. eq. 3.13), as the particles move with constant  $D$ -time velocity  $\mathbf{v}_n$  from  $D_n$  to  $D_{n+1/2}$  (see eq. 3.15a) – even if  $\mathbf{v}_n$  agrees to second order with 2LPT – because the change of the 2LPT velocity during this time interval is not taken into account in a DKD scheme. An auto-correction for this misplacement can however be applied on the fly, essentially by adjusting the weight functions  $(\alpha, \beta)$  appearing in the kick operation (eq. 3.15b), such that the velocity after the kick agrees again with the velocity truncated at order 2LPT, up to higher-order terms.

We will see that this adjustment also implies that the  $N$ -body particle positions conform to the 2LPT positions at that truncation order, and after each completed time step.

### 4.1 Initial time step

BULLFROG can be directly initialised at  $D = 0$  for step  $n = 0$ , which we discuss next. Note that the initialisation step is actually contained as a special case for the calculation for arbitrary  $n$  (section 4.2), and thus, nothing ‘special’ needs to be done for the initial step. From the perspective of a perturbative analysis, splitting up the initialisation step from the successive steps is however pedagogically constructive, and this is why we discuss it separately. Nonetheless, we refer fast readers not interested in this subtle difference to the next section, and in particular to eqs. (4.12) for the results.

The initial step  $n : 0 \rightarrow 1$  for  $D$ -time integrators assumes initial conditions of the type (3.19), which implies that particles are displaced according to the ZA during the first half drift. For the initial set of DKD operations, we have firstly (eqs. 3.15 with  $n = 0$ )

$$\mathbf{x}_{1/2} = \mathbf{q} + \frac{\Delta D}{2} \mathbf{v}_0, \quad (4.1a)$$

$$\mathbf{v}_1 = \alpha^{\text{BF}} \mathbf{v}_0 + \beta^{\text{BF}} [\Delta D/2]^{-1} \mathbf{A}(\mathbf{x}_{1/2}), \quad (4.1b)$$

$$\mathbf{x}_1 = \mathbf{x}_{1/2} + \frac{\Delta D}{2} \mathbf{v}_1, \quad (4.1c)$$

where  $\mathbf{x}_0 = \mathbf{q}$ , and  $\mathbf{v}_0 = -\nabla_{\mathbf{q}} \varphi^{\text{ini}}$  at  $D_0 = 0$  (cf. eq. 3.19), while  $(\alpha^{\text{BF}}, \beta^{\text{BF}})$  are the weights that we will derive in this section for the initial step. For this, we first need to calculate the gravitational acceleration  $\mathbf{A}(\mathbf{x}_{1/2})$  along the approximate particle trajectories, for which we consider

$$(\nabla_{\mathbf{x}} \cdot \mathbf{A})|_{\mathbf{x}=\mathbf{x}_{1/2}} = -\delta(\mathbf{x}_{1/2}). \quad (4.2)$$

Actually, since  $\mathbf{x}_{1/2}$  conforms to the ZA trajectory due to the choice of initial conditions, the given task is completely analogous to the one that we have already performed in section 3.1. Specifically, setting  $D = \Delta D/2$  in (3.12) and evaluating the expression along the discrete particle tracers, we have

$$\mathbf{A}(\mathbf{x}_{1/2}) = -\frac{\Delta D}{2} \nabla_{\mathbf{q}} \varphi^{\text{ini}} - \left(\frac{\Delta D}{2}\right)^2 \nabla_{\mathbf{q}}^{-1} \mu_2 + h.o.t., \quad (4.3)$$

where, again, we omit the particle labels for simplicity. Using this result as the input on the r.h.s. of the kick update (4.1b), as well as equating that expression with the truncated 2LPT velocity (3.7) evaluated at the completed time step  $D_1 = \Delta D$ , we obtain the following constraint equation which lies at the heart of BULLFROG,

$$\mathbf{v}^{\text{2LPT}}|_{D=\Delta D} = \left[-\nabla_{\mathbf{q}} \varphi^{\text{ini}} + \partial_D E \nabla_{\mathbf{q}}^{-1} \mu_2\right]|_{D=\Delta D} \stackrel{!}{=} -\alpha^{\text{BF}} \nabla_{\mathbf{q}} \varphi^{\text{ini}} - \beta^{\text{BF}} \left[\nabla_{\mathbf{q}} \varphi^{\text{ini}} + \frac{\Delta D}{2} \nabla_{\mathbf{q}}^{-1} \mu_2\right], \quad (4.4)$$

all of which is to be evaluated at the Lagrangian positions of the  $N$  tracer particles. Matching the coefficients of the  $\nabla_{\mathbf{q}} \varphi^{\text{ini}}$  terms leads to  $\alpha^{\text{BF}} + \beta^{\text{BF}} = 1$  implying the aforementioned ZA consistency; executing a similar matching for the 2LPT term then leads to

$$\alpha^{\text{BF}} = 1 + 2 \frac{E'_1}{\Delta D} = -\frac{5}{7} - \frac{30\Delta D^3 \Lambda}{1001} - \frac{15360\Delta D^6 \Lambda^2}{3556553} + O(\Delta D^9 \Lambda^3), \quad (4.5a)$$

$$\beta^{\text{BF}} = 1 - \alpha^{\text{BF}} = \frac{12}{7} + \frac{30\Delta D^3 \Lambda}{1001} + \frac{15360\Delta D^6 \Lambda^2}{3556553} + O(\Delta D^9 \Lambda^3), \quad (4.5b)$$

where  $E'_1 = [\partial_D E(D)]|_{D=\Delta D}$ . It is intriguing to compare these coefficients and their derivation with those of FASTPM and POWERFROG. All three integrators have in common that they are all ZA consistent, which is achieved when demanding  $\alpha + \beta = 1$ ; this is one of the two conditions required to fix the various  $D$ -time integrators. However, the three integrators are distinct from each other, as different conditions are imposed to fix the remaining condition. Specifically, for POWERFROG, its coefficients read  $\alpha^{\text{PF}} = -5/7$  and  $\beta^{\text{PF}} = 12/7$  for the initialisation step (cf. eq. 3.18), which are obtained by approximating  $E \simeq (-3/7)D^2$  in (4.4). By contrast, FASTPM was originally formulated in terms of canonical variables [70, Section 2.5], and their coefficient  $\alpha$  is kept the same as for the standard leapfrog integrator [96] (thus yielding symplecticity), while  $\beta$  is adjusted to ensure ZA consistency. In our notation, this leads to  $\alpha^{\text{FPM}} = \mathcal{F}_n/\mathcal{F}_{n+1}$  and  $\beta^{\text{FPM}} = 1 - \alpha^{\text{FPM}}$ , and one would therefore have  $\alpha^{\text{FPM}} = 0$  and  $\beta^{\text{FPM}} = 1$  for the initial step starting from  $D_0 = 0$ . Actually, as shown in ref. [72], FASTPM is the only  $D$ -time integrator that is ZA consistent as well as symplectic, while BULLFROG enforces 2LPT consistency instead; we will see later that BULLFROG generally comes with a better performance than FASTPM for predicting the LSS.

Finally, we need to verify that BULLFROG conforms to the 2LPT trajectories after the completed first time step. For this we plug the  $(\alpha^{\text{BF}}, \beta^{\text{BF}})$ -coefficients and the acceleration (4.3) into the kick (4.1b); using that expression in the second half-drift (4.1c) then leads to

$$\begin{aligned} \mathbf{x}_1 &= \mathbf{q} - \Delta D \nabla_{\mathbf{q}} \varphi^{\text{ini}} + \frac{\Delta D}{2} E'_1 \nabla_{\mathbf{q}}^{-1} \mu_2 + h.o.t. \\ &\stackrel{\text{EdS}}{\simeq} \mathbf{q} - \Delta a \nabla_{\mathbf{q}} \varphi^{\text{ini}} - \frac{3}{7} \Delta a^2 \nabla_{\mathbf{q}}^{-1} \mu_2 + h.o.t. \end{aligned} \quad (4.6)$$

By noting that  $E_1 = (\Delta D/2)E'_1 + O(\Delta D^5)$ , it becomes evident that this result agrees to second order with the 2LPT trajectory  $\mathbf{x}^{\text{2LPT}} = \mathbf{q} + \boldsymbol{\psi}^{\text{2LPT}}$  (eqs. 3.5) evaluated at  $D = \Delta D$ . ■

## 4.2 Arbitrary time steps

Next we consider all consecutive DKD steps  $n \rightarrow n+1$  for any  $n \geq 0$  (as noted above, the case  $n=0$  is actually also included). Assuming that the positions and velocities of the previous completed step  $n$  are 2LPT consistent, we will derive  $(\alpha^{\text{BF}}, \beta^{\text{BF}})$  in such a way that the same still holds after the  $(n+1)$ th step (provided that we are still in the pre-shell-crossing regime).

We begin by considering the first half-drift (3.15a), which for BULLFROG can be written as

$$\mathbf{x}_{n+1/2} = \mathbf{x}_n + \frac{\Delta D}{2} \mathbf{v}_n = \mathbf{q} - \left( D_n + \frac{\Delta D}{2} \right) \nabla_{\mathbf{q}} \varphi^{\text{ini}} + \left[ E_n + E'_n \frac{\Delta D}{2} \right] \nabla_{\mathbf{q}}^{-1} \mu_2 + h.o.t. \quad (4.7)$$

$$\stackrel{\text{EdS}}{\simeq} \mathbf{q} - \left( a_n + \frac{\Delta a}{2} \right) \nabla_{\mathbf{q}} \varphi^{\text{ini}} - \frac{3}{7} a_n (a_n + \Delta a) \nabla_{\mathbf{q}}^{-1} \mu_2 + h.o.t., \quad (4.8)$$

where, as a reminder,  $E_n = E(D)|_{D=D_n}$  and  $E'_n = (\partial_D E)|_{D=D_n}$ , and the second-order growth  $E$  is defined in eq. (3.5); furthermore, we note that, for the limiting case of uniform time stepping with  $\Delta D = \text{const.}$ , we have simply  $D_n = n\Delta D$  – here and below. It can be easily seen that the trajectory (4.7) does not agree with the corresponding trajectory in 2LPT (3.5) – not even in the EdS case – basically because the particles move on straight lines with velocity  $\mathbf{v}_n$  between time  $D_n$  and  $D_{n+1/2}$ , and the  $\mathbf{v}_n$  term in eq. (4.7) is therefore multiplied with just  $\Delta D/2$ .

The above implies that we need to determine the gravitational acceleration at slightly misplaced positions, for which we consider

$$(\nabla_{\mathbf{x}} \cdot \mathbf{A})|_{\mathbf{x}=\mathbf{x}_{n+1/2}} = -\delta(\mathbf{x}_{n+1/2}). \quad (4.9)$$

This equation can be solved with analogous perturbative techniques as discussed before, leading to

$$\mathbf{A}_{n+1/2} = - \left( D_n + \frac{\Delta D}{2} \right) \nabla_{\mathbf{q}} \varphi^{\text{ini}} + \left[ E_n + E'_n \frac{\Delta D}{2} - \left( D_n + \frac{\Delta D}{2} \right)^2 \right] \nabla_{\mathbf{q}}^{-1} \mu_2 + h.o.t. \quad (4.10)$$

$$\stackrel{\text{EdS}}{\simeq} - \left( a_n + \frac{\Delta a}{2} \right) \nabla_{\mathbf{q}} \varphi^{\text{ini}} - \left[ \frac{10}{7} a_n (a_n + \Delta a) + \frac{\Delta a^2}{4} \right] \nabla_{\mathbf{q}}^{-1} \mu_2 + h.o.t. \quad (4.11)$$

As expected, this result disagrees slightly with the 2LPT acceleration; cf. eq. (3.13) evaluated at  $D = D_n + \Delta D/2$ . This misplaced result needs to be taken into account in order to autocorrect the particle trajectory of the numerical integrator.

To do so, we plug the above results in the kick update (3.15b) and require that the kick coincide with the 2LPT velocity at the completed time  $D_{n+1} = D_n + \Delta D$  – this is the matching condition of BULLFROG executed at all time steps (cf. previous section where the same is done for the first step). The two individual conditions are easily evaluated, with the first being again  $\alpha^{\text{BF}} + \beta^{\text{BF}} = 1$  (now valid at all times) implying ZA consistency. Enforcing also 2LPT consistency then leads to our central result<sup>1</sup>

$$\alpha^{\text{BF}} = \frac{E'_{n+1} - F_{n+1/2}}{E'_n - F_{n+1/2}} \stackrel{\text{EdS}}{\simeq} \frac{4\mathfrak{n}(4\mathfrak{n}+1) - 5}{4\mathfrak{n}(4\mathfrak{n}+7) + 7}, \quad \beta^{\text{BF}} = 1 - \alpha^{\text{BF}} \stackrel{\text{EdS}}{\simeq} \frac{24\mathfrak{n} + 12}{4\mathfrak{n}(4\mathfrak{n}+7) + 7}, \quad (4.12a)$$

where  $\mathfrak{n} = a_n/\Delta a$  (which is equal to  $n$  for uniform time steps), and we have defined

$$F_{n+1/2} = D_{n+1/2}^{-1} (E_n + E'_n \Delta D/2) - D_{n+1/2}. \quad (4.12b)$$

To interpret the meaning of  $F_{n+1/2}$ , notice that the ratio between the source terms in the ODEs defining the second and first-order growth factors is given by  $(E - D^2)/D$  (see eqs. 3.5a and 3.5d), and  $F_{n+1/2}$  is the linearisation of exactly this ratio around  $D_n$ , evaluated at  $D_{n+1/2}$ . As promised, the calculations leading to (4.12) are actually not only valid for  $n > 0$ , but also for the ‘initialisation’ case with  $n = 0$ ,

basically since  $E_0 = 0 = E'_0$  and thus, the 2LPT growth terms do not contribute in the first drift at that time. Indeed, it is easy to verify that for  $n = 0$ , the weights (4.12) agree with those given in eqs. (4.5). Therefore, nothing ‘special’ has to be done for BULLFROG at initialisation time, and the coefficients (4.12) are valid at all times. We emphasise that BULLFROG and POWERFROG only agree for the first time step and for sufficiently early times, where both are 2LPT consistent. For later time steps, POWERFROG relies on weights derived from a transcendental equation to enforce second-order accuracy of the integrator. Furthermore, the second-order term of POWERFROG starts deviating from 2LPT for later time steps (section 5). By contrast, BULLFROG is 2LPT consistent at all time steps while automatically achieving second-order accuracy; see section 4.3 for details.

Equations (4.12) comprise the main results of the present section. To validate the calculation and to check for consistency, we plug the weights into the last half-drift update (3.15c) at time  $D_{n+1} = D_n + \Delta D$ , which yields after straightforward steps

$$\mathbf{x}_{n+1} = \mathbf{q} - (D_n + \Delta D) \nabla_{\mathbf{q}} \varphi^{\text{ini}} + \nabla_{\mathbf{q}}^{-1} \mu_2 \left[ E_n + \frac{\Delta D}{2} (E'_n + E'_{n+1}) \right] + h.o.t. \quad (4.13)$$

$$\stackrel{\text{EdS}}{\asymp} \mathbf{q} - (a_n + \Delta a) \nabla_{\mathbf{q}} \varphi^{\text{ini}} - \frac{3}{7} (a_n + \Delta a)^2 \nabla_{\mathbf{q}}^{-1} \mu_2 + h.o.t. \quad (4.14)$$

The square bracketed term in (4.13) amounts to a two-endpoint approximation for the integral in the formula  $E_{n+1} = E_n + \int_{D_n}^{D_{n+1}} E'(\tilde{D}) d\tilde{D} = E_n + (\Delta D/2) [E'_{n+1} + E'_n] + O(\Delta D^3)$ . Thus, eq. (4.13) agrees to second order with the 2LPT trajectory (3.5) evaluated at  $D_{n+1} = D_n + \Delta D$  as anticipated. ■

### 4.3 Numerical convergence

Here, we show that BULLFROG is second-order consistent with the standard symplectic DKD integrator as the time step  $\Delta D$  approaches zero. Provided that the gravitational force field is sufficiently smooth, this implies that BULLFROG is a globally second-order accurate scheme. However, we note that caustics affect the regularity of the force field [38], reducing the order of accuracy of *any* integrator in the post-shell-crossing regime; see ref. [72] for details.

As was shown in ref. [72, prop. 6], a  $D$ -time integrator is second-order accurate if  $\alpha + \beta = 1$  and, crucially, its  $\alpha$ -weight has a  $\Delta D$  expansion up to second order that agrees with the one of FASTPM<sup>2</sup> (eq. 3.16), i.e.,

$$\alpha^{\text{FPM}} = 1 - \alpha_1^{\text{FPM}} \Delta D + \alpha_2^{\text{FPM}} \Delta D^2 + O(\Delta D^3). \quad (4.15)$$

Here, the  $\Delta D$ -coefficients read

$$\alpha_1^{\text{FPM}} = \frac{\mathcal{F}'_n}{\mathcal{F}_n} \stackrel{\text{EdS}}{\asymp} \frac{3}{2a_n}, \quad \alpha_2^{\text{FPM}} = \frac{2\mathcal{F}_n'^2 - \mathcal{F}_n \mathcal{F}_n''}{2\mathcal{F}_n^2} \stackrel{\text{EdS}}{\asymp} \frac{15}{8a_n^2}, \quad (4.16)$$

and we remind the reader that  $\mathcal{F} = a^3 H \partial_a D$ . Of course, while all second-order accurate  $D$ -time integrators as defined in eqs. (3.15) must have the same  $\Delta D$ -coefficients up to second order, their higher-order coefficients are distinct among different integrators such as BULLFROG and FASTPM.

By contrast, expanding the  $\alpha$  of BULLFROG (eq. 4.12) about  $\Delta D = 0$ , we have

$$\alpha^{\text{BF}} = 1 - \alpha_1^{\text{BF}} \Delta D + \alpha_2^{\text{BF}} \Delta D^2 + O(\Delta D^3), \quad (4.17)$$

<sup>2</sup>The coefficient  $\alpha$  of FASTPM is identical to that of the standard leapfrog integrator when formulated in terms of  $(\mathbf{x}, \mathbf{v})$ ; however, the latter does not satisfy the ZA consistency condition  $\beta = 1 - \alpha$  in the kick, nor is its drift consistent with ZA.



with

$$\alpha_1^{\text{BF}} = DE''W^{-1}, \quad \alpha_2^{\text{BF}} = -[1/2] (DE''' + E'') W^{-1} - D^2 E'' W^{-2}, \quad (4.18)$$

where  $W := E - D(D + E')$  and from here on, the dependence  $D = D_n$  is implied and suppressed to ease the notation. Second-order accuracy of BULLFROG is achieved if both  $\alpha_1^{\text{BF}} = \alpha_1^{\text{FPM}}$  and  $\alpha_2^{\text{BF}} = \alpha_2^{\text{FPM}}$  are satisfied simultaneously.

Actually, although the  $\alpha_{1,2}^{\text{BF}}$  coefficients appear to be different from their reference values at first glance, we show analytically in the following that they coincide (see figure 5 for the numerical confirmation).

We begin with the proof related to  $\alpha_1$ , for which it is useful to first consider the  $D$ -time derivative of the definition  $\mathcal{F} = a^2 \dot{D}$ . Specifically, evaluating the temporal operator on the r.h.s. of  $\partial_D \mathcal{F} = \partial_D(a^2 \dot{D})$  and using the ODE for  $D$  to get an expression for  $\ddot{D}$  (see eq. 3.5), it is straightforward to verify the identity  $\partial_D \mathcal{F} = 3H_0^2 \Omega_{m0} a D / (2\mathcal{F})$ , from which it follows that  $\alpha_1^{\text{FPM}}$  can be written as

$$\alpha_1^{\text{FPM}} = \frac{3aD}{2\mathcal{F}^2}, \quad (4.19)$$

where  $\mathcal{F} := \mathcal{F} / (H_0 \Omega_{m0}^{1/2})$ . To get the BULLFROG weight  $\alpha_1^{\text{BF}}$  in the same form, it is useful to first rewrite the ODE for  $E$  (cf. eq. 3.5) as a function of  $D$ :

$$E'' = \frac{3aW}{2\mathcal{F}^2}, \quad (4.20)$$

where we used the definition of  $\mathcal{F}$  as well as the ODE for  $D$ . Plugging eq. (4.20) into  $\alpha_1^{\text{BF}}$  above, it is then easy to see that  $\alpha_1^{\text{BF}} = \alpha_1^{\text{FPM}}$ , which concludes the first part of the proof.

Next we proceed with the proof of  $\alpha_2^{\text{BF}} = \alpha_2^{\text{FPM}}$ , for which we note, using the before derived identity  $\partial_D \mathcal{F} = 3aD / (2\mathcal{F})$ , that we can rewrite the reference coefficient as

$$\alpha_2^{\text{FPM}} = \frac{3}{2} \left( \frac{\mathcal{F}'}{\mathcal{F}} \right)^2 - \frac{a'}{2a} \frac{\mathcal{F}'}{\mathcal{F}} - \frac{3}{4} \frac{a}{\mathcal{F}^2}. \quad (4.21)$$

To arrive at this end from the BULLFROG side, we need to evaluate  $E'''$ ; taking a  $D$ -time derivative from eq. (4.20), this task is simple, leading to  $DE''' = W\mathcal{F}'a' / (\mathcal{F}a) - 2D\mathcal{F}' / \mathcal{F} - 3W(\mathcal{F}' / \mathcal{F})^2$ , where  $W = E - D(D + E')$  as above. Using this as well as the above given identities, it is straightforward to confirm that  $\alpha_2^{\text{BF}} = \alpha_2^{\text{FPM}}$ ; thus, we conclude that BULLFROG is indeed second-order accurate. ■

We remark that the requirement of second-order accuracy is also achieved for POWERFROG (see ref. [72] for proofs); however, this requirement has to be explicitly built into the integrator, which involves solving numerically a transcendental equation (eq. 83 in ref. [72]). By contrast, the BULLFROG coefficients ( $\alpha^{\text{BF}}, \beta^{\text{BF}}$ ) – derived as the unique choice that yields 2LPT consistency after each step – naturally possess the asymptotic behaviour w.r.t.  $\Delta D$  required for second-order accuracy.

#### 4.4 Loss of convergence through approximate growth

It is important to emphasise that BULLFROG is only a consistent scheme if the actual  $\Lambda$ CDM growth functions are used, and not approximations thereof. This requires solving the ODEs for  $D$  and  $E$  either numerically (as we do) or analytically (i.e., by utilising the exact findings of ref. [81]). Indeed, if one instead employs the ‘ $D^n$  approximation’  $E \simeq (-3/7)D^2$  in the BULLFROG weight (dubbed ‘app’ in the following), one finds

$$\alpha^{\text{app}} = 1 - \alpha_1^{\text{app}} \Delta D + \alpha_2^{\text{app}} \Delta D^2 + O(\Delta D^3), \quad \alpha_1^{\text{app}} = \frac{3}{2D}, \quad \alpha_2^{\text{app}} = \frac{15}{8D^2}, \quad (4.22)$$

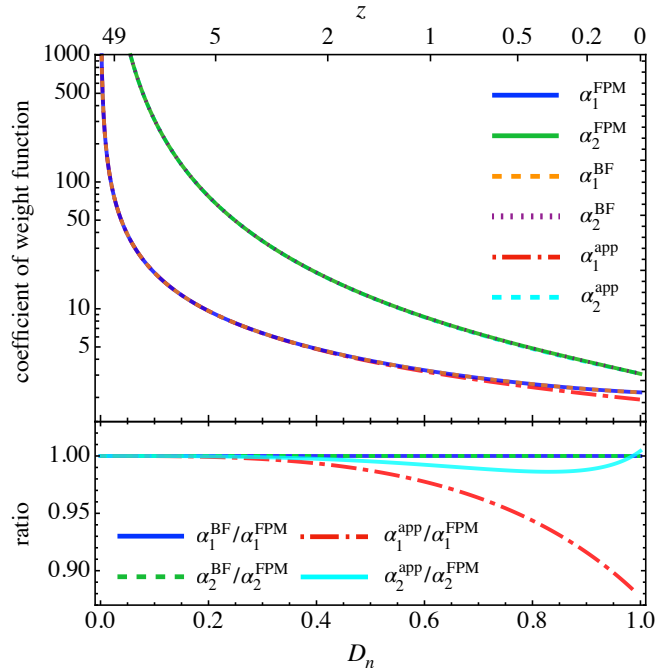


**Figure 5.** *Top panel:* Temporal evolution of the two  $\Delta D$ -coefficients  $\alpha_{1,2}^{\text{BF}}$  of BULLFROG (respectively shown in orange dashed and purple dotted lines), compared to the reference solutions for which we take FASTPM (solid blue and green lines). Second-order convergence is achieved for the BULLFROG coefficients, as they analytically agree with the reference coefficients. We also show approximate coefficients  $\alpha_{1,2}^{\text{app}}$  that arise if one ignores the explicit  $\Lambda$  dependencies in  $E$  (red dot-dashed and cyan dashed lines; the ‘ $D^n$  approximation’), which deviate from the reference for a vast range of times and therefore lead to an inconsistent scheme (section 4.4). We set  $\Lambda = 0.698/0.302$ , and, for convenience, we employ here the standard normalisation of the linear growth so that it is unity today. *Bottom panel:* Shown are ratios of the above coefficients versus the reference coefficients.

where  $D = D_n$  here and below. By contrast, if one formally expands the reference values about  $\Lambda = 0$ , one finds  $\alpha_1^{\text{FPM}} = 3/(2D) + (3/22)\Lambda D^2 + O(\Lambda^2)$  and  $\alpha_2^{\text{FPM}} = 15/(8D^2) + 3\Lambda D/44 + O(\Lambda^2)$ , i.e., *an infinite tower of  $\Lambda$  corrections*, which are completely ignored when using the  $D^n$  approximation. Since these terms already arise in  $\alpha_1$  (i.e. at linear order in  $\Delta D$ ), BULLFROG with the  $D^n$  approximation is not a consistent scheme, but instead only converges to an approximate solution. For similar reasons, convergence is also lost when employing the approximate second-order solution  $E \simeq -(3/7)\Omega_m^{-1/143}D^2 = -(3/7)D^2 - 3\Lambda D^5/1001 + O(D^8\Lambda^2)$  of ref. [29] (see also [97]), despite the fact that its  $\alpha_{1,2}$  coefficients would agree with the reference values up to  $O(\Lambda^2)$  analytically – and to within one percent numerically for a standard  $\Lambda$ CDM cosmology.

In figure 5 we show the evolution of the two  $\Delta D$ -coefficients  $\alpha_{1,2}$  as a function of the normalised growth, resulting from the benchmark considerations (solid blue and green lines), compared to the BULLFROG coefficients (orange dashed and purple dotted lines), as well as when employing the  $D^n$  approximation for BULLFROG (dot-dashed red and solid cyan lines). While the BULLFROG coefficients agree with the reference values, it is seen that the  $D^n$  approximations fare poorly at late times, preventing the integrator from converging to the correct solution as  $\Delta D \rightarrow 0$ .

Finally, in figure 6 we show the temporal evolution of  $\alpha = \alpha(\Delta D, D_n)$  as a function of  $\Delta D$  for  $D_n = 0.001, 0.1, 0.5$  (first three panels from left to right). In the first panel for  $D = 0.001$ , the black dotted line indicates the value  $\alpha = -5/7$ , required for 2LPT consistency. In contrast to the FASTPM integrator, both POWERFROG and BULLFROG have the correct 2LPT asymptotics at early

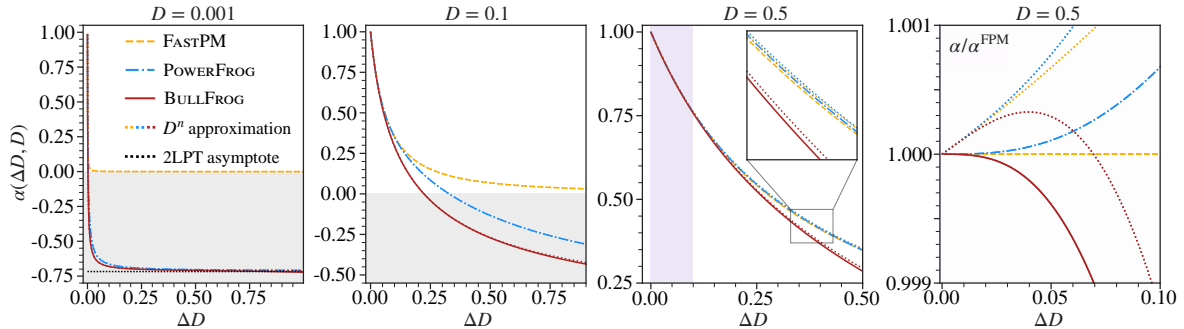


**Figure 6.** Weight  $\alpha$  for various  $D$ -time integrators as a function of step size  $\Delta D$ , respectively shown at the starting times  $D = 0.001, 0.1, 0.5$  in the first three panels (we normalise  $D$  and  $\Delta D$  as in the previous figure). BULLFROG (dark-red line) is 2LPT consistent about any starting time, which FASTPM (yellow dashed line) *never* achieves, and POWERFROG (blue dot-dashed line) only at early starting times for  $D \rightarrow 0$  (black dotted line). The  $D^n$  approximation of each  $\alpha$  (various dotted lines) does not converge towards the correct solution for  $\Delta D \rightarrow 0$ , as it is seen in the rightmost panel, which shows the ratio  $\alpha/\alpha^{\text{FPM}}$  as a function of  $\Delta D$  for  $D = 0.5$  (in the purple-shaded time-step range from the third panel): A consistent method that is second-order accurate amounts to  $\alpha/\alpha^{\text{FPM}} = 1 + O(\Delta D^3)$ , which is achieved for the considered  $D$ -time integrators, but not when approximative growth functions are used, due to ‘forbidden’ contributions of  $O(\Delta D)$ . The grey shaded area indicates the regime when  $\alpha < 0$ , implying that the Hubble drag acts so strongly during the time step that the direction of the current velocity is *reversed* before adding the acceleration in the kick (see eq. 3.15b).

times. However, BULLFROG – which matches the 2LPT term at *all* times prior to shell-crossing – prefers smaller values for the  $\alpha$ -weight than POWERFROG at later times. The dotted lines show the respective  $D^n$  approximation for a given weight. At early times, these approximations closely follow their full  $\Lambda$ CDM counterparts; however, as discussed above, they do *not* lead to consistent methods and hence do not converge towards the correct solution for  $\Delta D \rightarrow 0$ . This becomes clear from the rightmost panel, which shows the ratio of  $\alpha$  to  $\alpha^{\text{FPM}}$  for each stepper, for  $D = 0.5$  and the range of time steps  $\Delta D$  shaded purple in the previous panel. While the  $\Lambda$ CDM coefficients all have the same asymptotic behaviour up to second order for  $\Delta D \rightarrow 0$  (thus yielding second-order accurate methods, see ref. [72]), already the linear term of the  $D^n$  approximations differs.

## 5 Implementation and results

We perform two distinct numerical experiments to demonstrate the effectiveness of BULLFROG. For the first experiment, we examine the case of filtered initial conditions with a sharp UV cutoff in Fourier space, which sets all Fourier modes with  $|\mathbf{k}| > k_\Lambda$  to zero (section 5.2). This filtering removes small-scale information from the initial conditions, which significantly delays the instance of first shell-crossing in the resulting coarse-grained/smoothed fluid: Without smoothing, and under the present simulation settings (section 5.1), the first shell-crossing occurs around  $z \simeq 5$ , while with UV cutoff at  $k_\Lambda = 0.2 h \text{ Mpc}^{-1}$ , this event is delayed to  $z \simeq 2$  (see figure 7). If the filter is instead set at  $k_\Lambda = 0.1 h \text{ Mpc}^{-1}$ , the first shell-crossing occurs just shortly before  $z = 0$ . Thus, the applied filtering technique extends the validity of LPT (which becomes unreliable when  $J < 0$  for the first time) in  $\Lambda$ CDM, enabling us to perform controlled experiments. From an application point of view, investigating the evolution of coarse-grained fluids is interesting because it opens up the possibility of using BULLFROG instead of high-order LPT as a fast, less memory-intensive, and easy-to-implement forward model in hybrid approaches that leverage techniques of effective field theory for the small-scale modelling (see e.g. [48, 78, 80, 98] for related avenues).

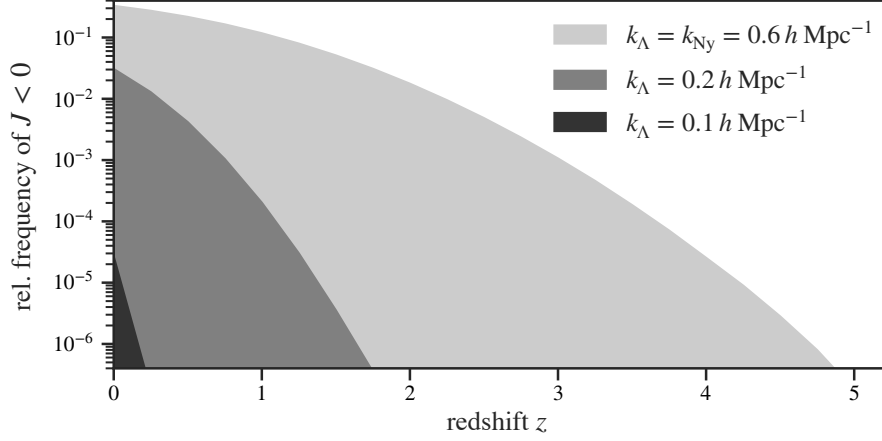


**Figure 7.** Fraction of particles with a negative Jacobian determinant  $J(\mathbf{x}(\mathbf{q}, z)) < 0$  as a function of redshift  $z$ , computed with 3LPT. Recall that  $J$  is positive at early times (as  $\mathbf{x} \rightarrow \mathbf{q}$  for  $z \rightarrow \infty$ ) and crosses zero from above at the instant of shell-crossing. For the present choice of simulation settings and without UV cutoff (*‘unfiltered’*, light grey; section 5.3), the first shell-crossing occurs around  $z \simeq 5$ , marking the point when LPT starts losing its validity, and more than 30% of the particles have  $J < 0$  at  $z = 0$ . For the filtered cases with a cutoff at  $k_\Lambda = 0.2 h \text{ Mpc}^{-1}$  (medium grey; section 5.2), the first shell-crossing occurs delayed at about  $z \simeq 2$ , while with  $k_\Lambda = 0.1 h \text{ Mpc}^{-1}$  (dark grey), almost the whole simulation domain is still single stream at  $z = 0$ . This figure provides a rough rule of thumb for estimating how many particles participate in multi-streaming.

	LPT	Standard leapfrog	COLA	FASTPM (FPM)	BULLFROG (BF)
UV complete	✗	✓	✓	✓	✓
Accurate with few orders / steps	✓	✗	✓ – ✓*	✓	✓
Memory-friendly	✗	✓	~	✓	✓
2LPT consistent	n.a.	✗	✓	✗	✓
No additional hyperparameters	✓	✓	✗	✓	✓
No need for LPT-based ICs	n.a.	✗	✗	✓ <sup>†</sup>	✓
No spatial discreteness errors	✓	✗	✗	✗	✗ <sup>‡</sup>

\* With COLA, we find large variations in the accuracy depending on the choice of the  $n_{\text{LPT}}$  hyperparameter.

<sup>†</sup> FASTPM can be initialised directly at  $a = 0$ ; however, the mismatch in the 2LPT term hampers its accuracy in this case.

<sup>‡</sup> BULLFROG is no different from the other integrators regarding spatial and force-related properties, which is why in this work, we employ discreteness reduction schemes, see the main text.

**Table 1.** An overview of the pros and cons of the employed forward models. LPT is highly accurate and does not suffer from spatial discreteness; however, it is not UV complete, as it does not incorporate shell-crossing. Additionally, calculating the LPT displacement is computationally prohibitive at higher orders. By contrast, the standard leapfrog integrator is oblivious to LPT insights and requires small time steps in order to capture the dynamics on linear scales, thus unnecessarily wasting precious computing resources at high redshifts. This issue is rectified when employing the  $D$ -time integrators FASTPM and BULLFROG, which are respectively ZA and 2LPT consistent. Note that POWERFROG (not listed in table) differs from BULLFROG in that it conforms with 2LPT only asymptotically for  $a \rightarrow 0$ , and otherwise is ZA consistent. The modified COLA algorithm of ref. [68] can achieve a high level of accuracy in fast predictions of the LSS. In contrast to  $D$ -time integrators, COLA explicitly computes the 2LPT trajectories (which must be kept in memory during the simulation runtime) and corrects them by adding a residual, determined in an  $N$ -body fashion. Achieving optimal performance with COLA requires fine-tuning of the ‘ $n_{\text{LPT}}$  hyperparameter’ (see footnote 3) through trial and error.

For the second experiment, we consider standard/unfiltered initial conditions in  $\Lambda$ CDM, focusing on comparing BULLFROG to other methods; see section 5.3 as well as table 1 for an overview of the forward models considered. Apart from FASTPM, we also test against COLA which is not a  $D$ -time integrator. Instead, it incorporates 2LPT into a standard leapfrog integrator by explicitly shifting the phase-space coordinates to those of a ‘2LPT observer,’ and then solving for the residual between the true trajectories and 2LPT [68, 69, 69, 99, 100]. COLA requires explicitly computing the 2LPT displacement, which must be stored in memory throughout the simulation. We employ the modified time stepper of the COLA algorithm (see appendix A.3.2 in ref. [68]), since it reportedly performs better than its base stepping scheme. The modified COLA scheme introduces an additional hyperparameter,  $n_{\text{LPT}}$ , which delicately affects the results (see, e.g., refs. [69, 70] and our findings below).<sup>3</sup> The authors of COLA recommend values for  $n_{\text{LPT}}$  ranging between  $-4$  and  $3.5$ , but do not provide explicit instructions for selecting the optimal value, as it can depend non-trivially on factors such as initialisation redshift, box size, force resolution, particle masses, and even subtleties such as the exact procedure for generating the initial conditions. Instead, users should choose an optimal value for  $n_{\text{LPT}}$  through trial and error.

## 5.1 Numerical implementation

Here we provide details of the experimental setup and the numerical implementation of the various methods. Unless stated differently, we consider a simulation box of edge length  $L = 2 \text{ Gpc}/h$ , use  $384^3$   $N$ -body particles with a grid resolution of  $768^3$  for the force computation with the PM method, and perform computations in double precision on a single GPU. We do not employ any force softening. We take the cosmology to be spatially flat  $\Lambda$ CDM with  $\Omega_{\text{m}0} = 0.302$ ,  $H_0 = 67.7 \text{ km/s/Mpc}$ ,  $n_s = 0.968$ , and  $\sigma_8 = 0.815$ .

Throughout the results section, we will use the shorthand notation  $n\text{BF}$  to denote  $n$  time steps executed with BULLFROG, and similarly for POWERFROG (PF), FASTPM (FPM), and COLA. For  $D$ -time integrators, we only employ  $D$ -time spacing uniformly distributed between 0 and 1 for simplicity. For COLA (which, recall, is not a  $D$ -time integrator), we employ linear-in- $a$  steps as in the original COLA paper [68], and we use the ‘modified’ COLA scheme in KDK form as described in their appendix A.3.2 which, according to the authors, performs better than their ‘standard’ scheme (appendix A.3.1; cf. the findings of [69, 99]). It is likely that further performance gains from all fast integrator methods can be achieved by adopting refined time-stepping strategies, which however requires further investigation.

We implemented all numerical integrators, including specifically COLA, within the same code ecosystem. This has the added benefit of ensuring that force computations are identical across all integrators, allowing us to study the intrinsic properties of the time integrators in isolation. Furthermore, to mitigate the discrete nature of  $N$ -body simulations, we employ several discreteness reduction schemes. Specifically, we use Fourier sheet interpolation [101, 102], the exact Fourier gradient kernel  $i\mathbf{k}$ , higher-order mass assignment [103], and de-aliasing via grid interlacing [104] to improve the accuracy of the force computation; see ref. [73] for details of all these techniques. While we use these techniques at all times for the filtered simulations, we choose to disable them after redshift  $z = 25$  for the unfiltered  $\Lambda$ CDM simulations when the impact of discreteness effects is already

---

<sup>3</sup>The  $n_{\text{LPT}}$  parameter in COLA modifies the temporal weights of the residual terms solved by the  $N$ -body method, which the authors of ref. [68] suggest is connected to the exponent of any of the six growing and decaying modes that emerge at third order in LPT. However, we respectfully question this justification for the following reasons: (1) Before shell-crossing and using growing-mode initial conditions, the  $N$ -body residual aligns with the fastest growing mode (modulo discreteness errors), which would make the selection of  $n_{\text{LPT}}$  unnecessary (in the continuum limit); (2) after shell-crossing, when LPT becomes invalid, the residual is in general not of the 3LPT type, and therefore, none of the growing or decaying modes of 3LPT should be physically relevant in that regime. We conjecture that the observed performance gain from adjusting  $n_{\text{LPT}}$  may stem from a better control of spatial discreteness errors, though further research is needed to confirm this hypothesis.

significantly lower than at early times. This is mainly for reasons of computational efficiency, but we also note that these techniques should anyhow not be used (without spatial refinement) in scenarios where the phase-space sheet is highly complex, i.e. on highly nonlinear scales [101, 102].

For the LPT implementation, we generate the displacement fields exploiting the recursive relations from ref. [35] and de-alias them using Orszag’s 3/2 rule [105]. We have also tested the computationally expensive ‘leave-no-mode-behind’ method explained in ref. [80] (see also [106, 107]), which takes into account mode-couplings beyond the original UV cutoff. However, we found negligible impact within our setup and therefore ignore this subtle effect for computational ease. By contrast, we include transverse contributions to the displacement, which were ignored in the results presented in ref. [80]; including these transverse fields is computationally expensive (see below) but introduces a two-loop effect (and higher) to the matter power spectrum, and a one-loop effect to the matter bispectrum [108]. Regarding the temporal evolution of the LPT displacement, we perform a single time step from  $z = \infty$  to the target redshift, and employ two different schemes: (1) the commonly used ‘ $D^n$  approximation’ for modelling the LPT growth at order  $n$  (sometimes called ‘[quasi-]EdS approximation;’ see e.g. refs. [47, 97, 109]), and (2) the exact growth based on numerical solutions of the underlying ordinary differential equations up to third order in LPT, with a switch to the  $D^n$  approximation for  $n$ LPT when  $n > 3$ . We remark that using the actual  $\Lambda$ CDM displacement growth is ultimately prohibitive at large LPT orders, since the number of spatial terms increases greatly with the order, but must be kept in storage; see ref. [80] for a related implementation of the LPT recursion relation. To determine the Eulerian density field given the current particle positions  $\mathbf{x}(\mathbf{q}, t)$ , obtained with a numerical integrator or with LPT, we compute a cloud-in-cell approximation of the exact overdensity

$$\delta(\mathbf{x}, t) + 1 = \int_{(L\mathbb{T})^3} \delta_{\text{D}}(\mathbf{x} - \mathbf{x}(\mathbf{q}, t)) \, \text{d}^3q, \quad (5.1)$$

where  $\delta_{\text{D}}$  is the Dirac delta, and  $(L\mathbb{T})^3$  denotes the three-dimensional torus of side length  $L$ . In the following, we will also show results for the matter power spectrum  $P$ , which we define with

$$\langle \tilde{\delta}(\mathbf{k}_1) \tilde{\delta}(\mathbf{k}_2) \rangle = (2\pi)^3 \delta_{\text{D}}(\mathbf{k}_1 + \mathbf{k}_2) P(k_1), \quad (5.2)$$

where  $k = |\mathbf{k}|$ , and the tilde denotes a Fourier transform with respect to the Eulerian coordinate.

## 5.2 Simulations with UV cutoff

We begin by reporting the results for the case where a sharp UV cutoff in Fourier space is applied to the initial conditions, which is relevant for the study of effective fluids. In figure 8 we show ratios of power spectra with respect to a reference simulation done with 50BF, where the latter is well converged for the cutoff choices  $k_{\Lambda} = 0.1 \, h \, \text{Mpc}^{-1}$  (top panels) and  $k_{\Lambda} = 0.2 \, h \, \text{Mpc}^{-1}$  (bottom panels), evaluated at  $z = 0$ . The left panels compare BULLFROG (shown in red) with LPT (other colours) results. For BULLFROG, the various line styles denote the number of time steps, while for LPT, the line styles designate whether the growth ODEs were solved exactly (solid), or whether the  $D^n$ -approximation was used (dotted); note that for LPT orders  $> 3$ , we always use the  $D^n$ -approximation (dot-dashed).

For the lower cutoff ( $k_{\Lambda} = 0.1 \, h \, \text{Mpc}^{-1}$ ), LPT converges towards the reference result when consecutively increasing the perturbation order. This is expected, as almost the whole spatial domain of the effective fluid is still single stream (see figure 7), in which case LPT should be fairly accurate. However, the accuracy of LPT comes at a high computational price: achieving 0.25% accuracy with the lower cutoff choice requires 5LPT, which comes with a whopping 17 spatial kernels in the scalar sector and with 7 transverse contributions in the vector sector. Asymptotically, the number of new terms at each order grows quadratically, making high-order LPT prohibitively expensive in terms of

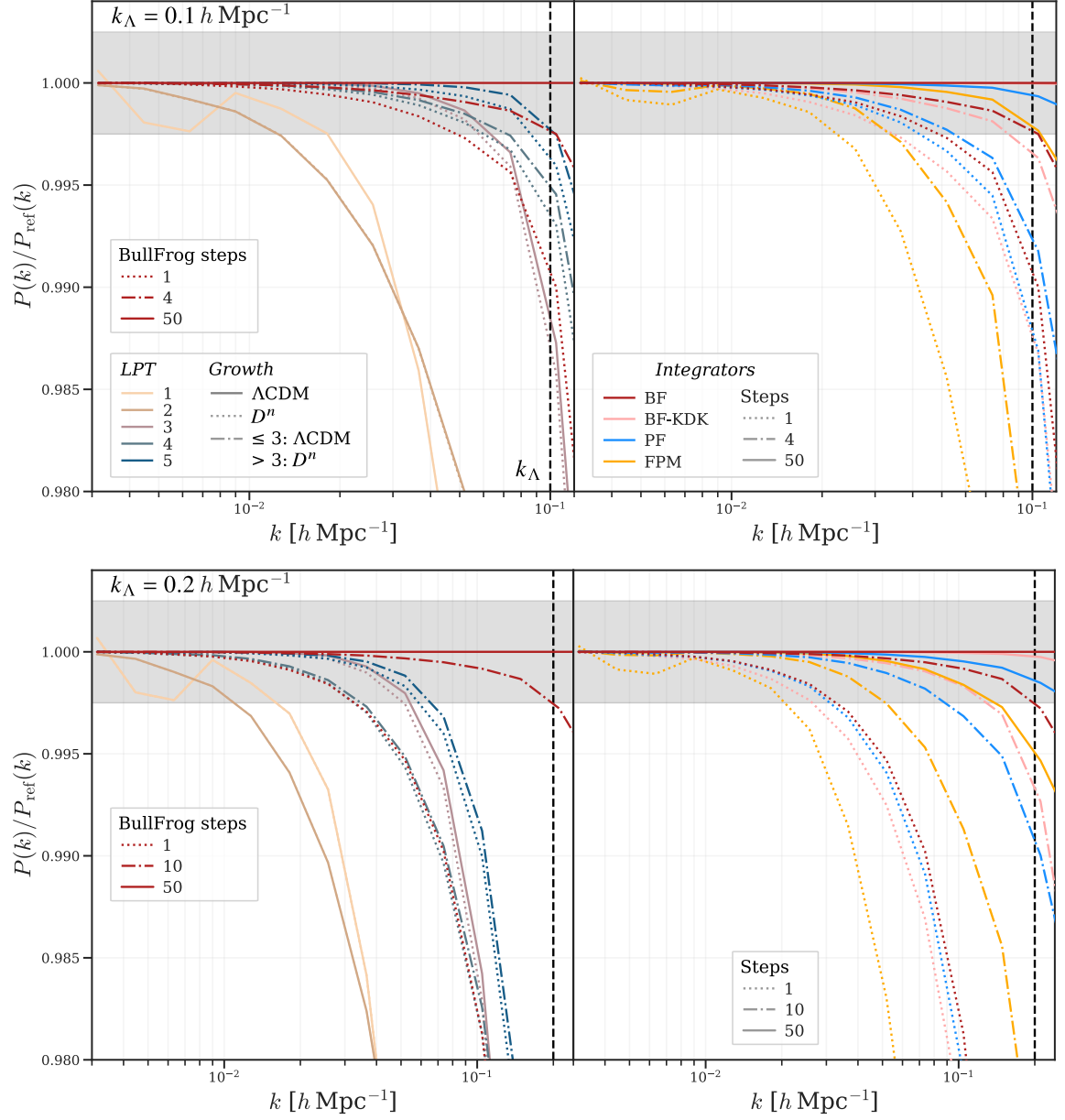


**Figure 8.** Today’s matter power spectrum relative to the BULLFROG prediction with 50 steps (50BF). In the upper [lower] panels, the cutoff scale in the ICs is  $k_\Lambda = 0.1$  [ $0.2$ ]  $h \text{ Mpc}^{-1}$ . All integrators were initialised at  $z = \infty$ , and the discreteness suppression was active for the whole runtime. The left panels show a comparison of BF with LPT (see main text for the explanation of the growth). For both cutoffs, already a single BF step is better than 2LPT. For  $k_\Lambda = 0.1 h \text{ Mpc}^{-1}$ , where LPT converges well to the reference solution, the performance of 4BF lies between 4 – 5LPT, with an error of about 0.25% (grey band) at  $k_\Lambda$ . For the case of  $k_\Lambda = 0.2 h \text{ Mpc}^{-1}$ , the power of high-order LPT drops off already well above  $k_\Lambda$ , as shell-crossing physics becomes relevant but is not incorporated. By contrast, 10BF is sufficient to keep the error below 0.25% up to  $k_\Lambda$ . In the right panels, we show results for the KDK variant of BULLFROG (BF-KDK; see appendix A), POWERFROG (PF), and FASTPM (FPM). The loss of power with 4BF for  $k_\Lambda = 0.1 h \text{ Mpc}^{-1}$  is comparable to 50FPM, and 10BF outperforms 50FPM for the case with  $k_\Lambda = 0.2 h \text{ Mpc}^{-1}$ . BULLFROG also improves on POWERFROG in all cases.

memory and computing time. Also, at such late times, the actual  $\Lambda$ CDM growth should be taken into account, although we find that the effect is fairly subtle up to third order (see [80] for incorporating the actual growths at larger orders). By contrast, 4BF is already converged up to 0.25% accuracy for the lower cutoff, and even 1BF fares significantly better than 2LPT – and is almost as good as 3LPT.

A crucial advantage of  $n$ BF over  $n$ LPT is its constant memory footprint when increasing the number of steps  $n$  (unlike when increasing the order  $n$  in the case of LPT). Indeed, when using BULLFROG as a time integrator, only two arrays of size  $N$  (for positions and momenta) are required in principle, along with the resources for force computation, such as a PM grid, just as in any standard  $N$ -body simulation. The positions and momenta are updated in place by the drift and kick operation, respectively. That said, depending on the desired level of accuracy, the use of discreteness suppression techniques is advisable at early times (see section 5.1), which leads to an increase in runtime and memory (and obviously to more internal parameters that need to be adjusted). However, we remark that the use of discreteness suppression schemes can be circumvented if the simulation is initialised at sufficiently late times using 2 – 3LPT [73, 83] – and for fast approximate simulations, these techniques might be omitted altogether even when starting at  $D = 0$ .

For the higher cutoff case with  $k_\Lambda = 0.2 h \text{Mpc}^{-1}$ , we observe emerging non-convergent behaviour of LPT (bottom-left panel in figure 8): 4LPT performs slightly worse than 3LPT with respect to the reference result, while 5LPT comes only with a minor improvement; see also ref. [80] for similar observations. The weaker LPT performance can be explained by the fact that significantly more particles have shell-crossed by  $z = 0$  as compared to the lower cutoff case (figure 7). Consequently, it is questionable whether higher-order LPT predictions could significantly alleviate the observed discrepancy, as shell-crossing physics becomes relevant and should be incorporated. By contrast, BULLFROG, being a UV-complete method, converges to the correct solution also after shell-crossing. In fact, we find that already 10BF yields an error of less than 0.25% w.r.t. the reference result for  $k \leq k_\Lambda$ .

In the right panels of figure 8, we compare BULLFROG against various  $D$ -time integrators, all initialised at  $a = 0$ . Regarding the KDK version of BULLFROG (BF-KDK; pink lines in figure 8), the late-time performance is fairly comparable to its DKD version, but we note that BF-KDK was initialised at  $a = 0$  using 1BF(-DKD), for reasons explained in appendix A. FASTPM (i.e., its DKD variant) [72], by contrast, does not perform so well. This can be explained by the fact that FASTPM is only Zel’dovich consistent, which is a disadvantage particularly when initialised at  $a = 0$ . This weakness of FASTPM could be slightly mitigated by initialising with, for example, 2LPT or using the DKD variant of BF. Nonetheless, despite such a ‘jump start,’ FASTPM introduces a 2LPT error from its first step onwards, causing it to converge significantly more slowly than BULLFROG (see figure 13).

In figure 9 we compare BULLFROG against various settings within COLA for the cutoff case  $k_\Lambda = 0.1 h \text{Mpc}^{-1}$ . The panels from left to right show COLA results initialised at  $z_{\text{ini}} = 49, 24,$  and  $9$ . The various line styles indicate different linear-in- $a$  steps (as recommended by the developers), while the three colours denote three choices of the hyperparameter  $n_{\text{LPT}}$ . For all presented combinations of hyperparameters and initialisation redshifts, COLA converges to the benchmark solution. For a low number of time steps, however, COLA results depend weakly on the initialisation redshift and strongly on the chosen hyperparameter. Notably, among the three considered choices, we find  $n_{\text{LPT}} = 3.5$  performs best in this scenario, which is quite different from the default value of  $n_{\text{LPT}} = -2.5$  adopted in refs. [68, 69] (the latter value yields favourable results in our experiment without an IC cutoff with 10 steps, however only when starting at  $z_{\text{ini}} = 9$ ; see figure 12).

As a final exercise, and to connect to the full simulations as performed in the following section, we determine the effective speed of sound of matter,  $c_s$ , which we define through

$$P_{\text{full}}(k, t) = [1 - 2c_s^2(k, t; k_\Lambda)k^2] P_\Lambda(k, t) \quad \Leftrightarrow \quad c_s^2(k, t; k_\Lambda) = \frac{P_\Lambda(k, t) - P_{\text{full}}(k, t)}{2k^2 P_\Lambda(k, t)}. \quad (5.3)$$



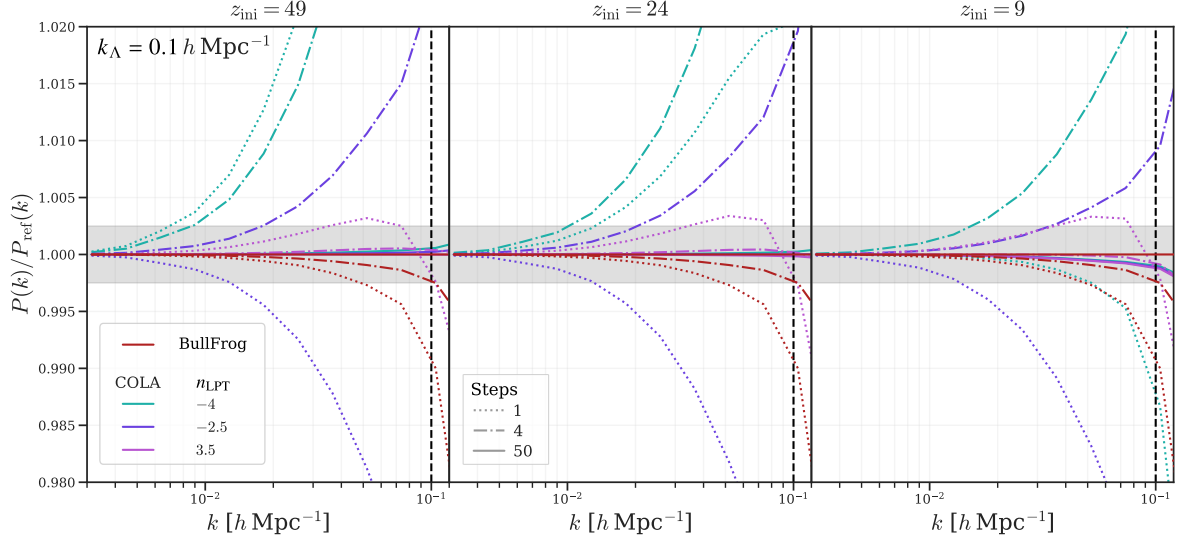


**Figure 9.** Same BULLFROG power spectra as in figure 8, but now in comparison with COLA time stepping, for three different COLA hyperparameters ‘ $n_{\text{LPT}}$ ’ (various colours) and three different redshifts for initialising COLA with 2LPT (from left to right).<sup>3</sup> The COLA power spectra are highly sensitive to the choice of  $n_{\text{LPT}}$  and can overshoot already with a single step. BULLFROG yields results competitive with the best-performing choice of  $n_{\text{LPT}}$  in COLA (here:  $n_{\text{LPT}} = 3.5$ ), converges monotonically from below in terms of power as the number of steps increases, and does not require the computation of spatial 2LPT kernels.

Here,  $P_{\Lambda}(k, t)$  is the power spectrum with cutoff at  $k_{\Lambda}$  in the ICs, determined using either  $n\text{LPT}$  or  $n\text{BF}$  as above, while  $P_{\text{full}}$  denotes a converged simulation result without cutoff. In the following, we compute  $P_{\text{full}}$  using a 100BF simulation with Nyquist scale  $k_{\text{Ny}} = 0.6 h \text{ Mpc}^{-1}$ . Physically,  $c_s^2$  reflects a contribution to the power spectrum from small-scale physics with modes  $k > k_{\Lambda}$  which, through nonlinear mode coupling, affects also the large-scale modes with  $k \leq k_{\Lambda}$ . Within the effective field theory (EFT) framework,  $c_s^2$  is the leading-order counterterm if it is scale independent, while residual scale-dependency can be interpreted as higher-order- or EFT counterterm corrections [42, 44]; see refs. [80, 110] for similar results based on eq. (5.3) where, however,  $P_{\Lambda}$  is taken solely from  $n\text{LPT}$ .

Figure 10 shows the predictions for  $c_s^2$ , with the same colour and line styles as used in figure 8. The left panel displays the results for the lower cutoff ( $k_{\Lambda} = 0.1 h \text{ Mpc}^{-1}$ ), and the right panel for the higher cutoff ( $k_{\Lambda} = 0.2 h \text{ Mpc}^{-1}$ ). For both cutoffs and for both the BULLFROG and LPT predictions, we observe a drop in power of  $c_s^2$  for  $k$ -values approaching  $k_{\Lambda}$  from below. Within an EFT, as argued by refs. [80, 110], this behaviour is expected because, in the current implementation,  $c_s^2$  must capture all nonlinear mode couplings, which become non-trivial near the cutoff scale. This scale dependency in  $c_s^2$  could be suppressed by including terms of  $O([k/k_{\Lambda}]^4)$  in the relationship between  $P_{\Lambda}$  and  $P_{\text{full}}$ . In contrast, on large scales, sufficiently far from the cutoff, the BULLFROG results for  $c_s^2$  form a plateau of roughly constant height for any number of time steps, indicating that a single and  $k$ -independent counterterm adequately captures the UV feedback on the power spectrum at scales  $k \ll k_{\Lambda}$ , at least for the present choices of cutoffs.

Regarding the LPT results with the lower cutoff (left panel in figure 10), we observe a similar convergence of  $n\text{LPT}$  at increasing perturbation orders as previously noted (see top-left panel of figure 8 and [80]). However, the aforementioned scale independence for  $k \ll k_{\Lambda}$  becomes pronounced only for orders  $n \gtrsim 3$ , whereas 1–2 LPT leads to (unphysical) negative values of  $c_s^2$  (see also [80]). By contrast, for the larger cutoff (right panel in figure 10), the scale independence is not even reached

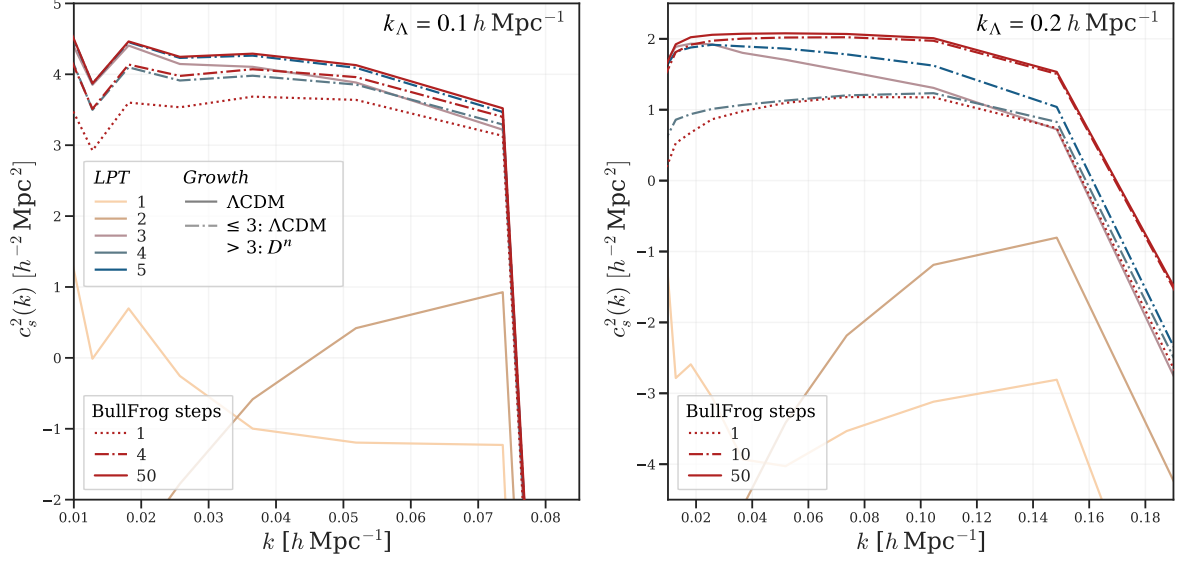


**Figure 10.** Speed of sound  $c_s^2$  as defined through eq. (5.3), using either  $n$ LPT or  $n$ BF as the forward model, adopting the same line styles as in figure 8. The left [right] panel shows results for  $k_\Lambda = 0.1[0.2] h \text{ Mpc}^{-1}$ . The BF predictions are approximately constant for sufficiently large scales, indicating that  $c_s^2$  can be identified with the leading-order EFT counterterm for the present choices of  $k_\Lambda$ .

by 5LPT, which in the present case is explained by the impending loss of perturbative control. Indeed, the 4LPT prediction performs worse than 3LPT in comparison to the reference result, indicating that LPT convergence is lost on the considered scales (cf. bottom-left panel of figure 8). In this context, we remark that it is well documented that both field-level and power-spectrum predictions of LPT converge monotonically within its validity regime; see e.g. refs. [33–36, 41, 83].

In conclusion, among all tested forward models, BULLFROG provides the fastest and most reliable LSS predictions with cutoff. For sufficiently small cutoffs ( $k_\Lambda \lesssim 0.1 h \text{ Mpc}^{-1}$ ), where  $n$ LPT predictions are very accurate for  $n \geq 4$  down to  $z = 0$ , we find good agreement with all tested  $N$ -body integrators, with BULLFROG requiring the fewest time steps for reaching a given target accuracy.

### 5.3 Full $\Lambda$ CDM simulations

We now turn to full  $\Lambda$ CDM simulations without cutoff, extending down to the Nyquist scale  $k_{\text{Ny}} = \pi N^{1/3} L^{-1} \simeq 0.6 h \text{ Mpc}^{-1}$  (and slightly beyond due to corner modes  $|\mathbf{k}| > k_{\text{Ny}}$  that we include); see section 5.1 for details on the numerical setup. Figure 11 shows ratios of power spectra relative to the reference run, obtained with 100BF. The left panel compares  $n$ BF with  $n$ LPT predictions, adopting the same colour and line styles as in figure 8. Unsurprisingly, LPT convergence is lost at such late times (cf. figure 7), which is exemplified by a significant loss in power on a vast range of nonlinear scales. For example, at  $k_{\text{Ny}}$ , the accuracy of the power-spectrum prediction of 3LPT [5LPT] deviates by 66.36% [69.14%] from the reference result. BULLFROG, on the other hand, yields predictions that are accurate to 0.33% and better for  $n \gtrsim 10$ .

In the right panel of figure 11, we compare the BULLFROG results with the other  $D$ -time integrators, and against a standard symplectic integrator initialised at the two redshifts  $z = 127, 49$  with 2LPT. Like BULLFROG, the symplectic integrator is UV-complete in the temporal sense, ensuring that it consistently yields the correct solution in the limit of vanishing time steps, unaffected by shell-crossing. However, the symplectic integrator entirely overlooks the accurate description of structure growth provided by LPT at early times and on large scales, necessitating small time steps to capture

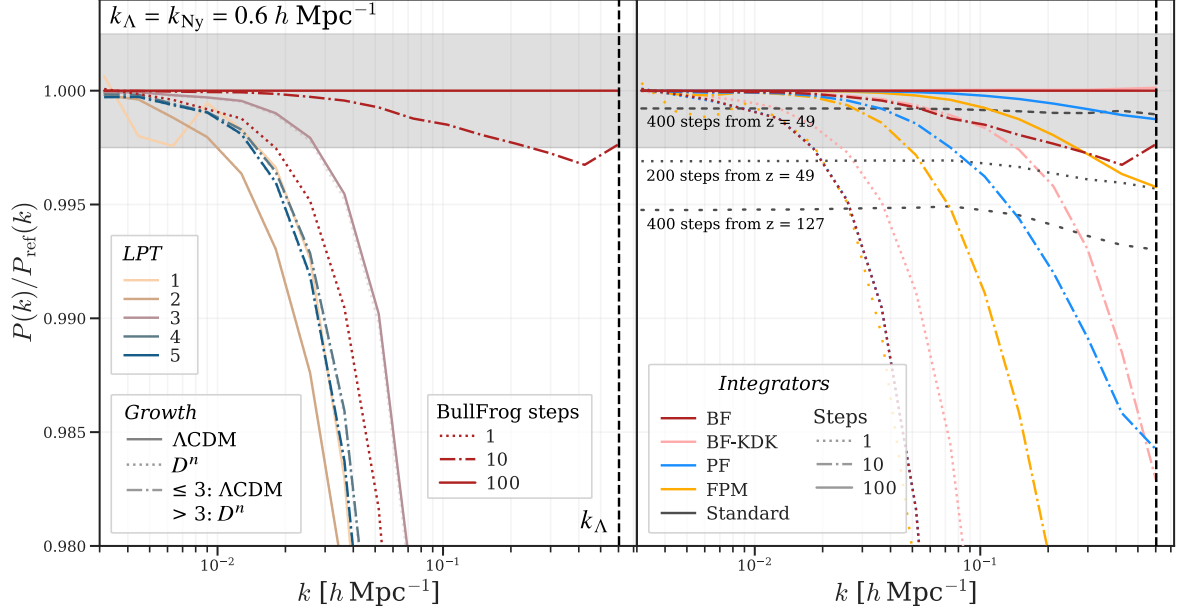


**Figure 11.** Similar as figure 8, but now showing results for full  $\Lambda$ CDM simulations at  $z = 0$ . The  $D$ -time integrators were initialised at  $z = \infty$  with discreteness suppression techniques switched off at  $z = 25$ . We also present results using a standard symplectic (DKD) leapfrog integrator (also with discreteness suppression), initialised with 2LPT at  $z = 49$  or  $z = 127$ , whose convergence is very slow because even the leading-order ZA dynamics are only recovered in the limit  $\Delta D \rightarrow 0$ .

the dynamics on linear scales, which in turn wastes valuable computing resources at high redshifts. Specifically, even with hundreds of time steps, an (admittedly small) residual in the power spectrum remains, which is remarkably constant as a function of scale and converges very slowly. We have explicitly verified that this residual can be further reduced by a late-time initialisation using 3LPT at  $z = 24$ , where the 200-step result already has an edge over the 400-step result with the 2LPT initialisation at  $z = 49$  (not shown; see also [83]). Regarding the  $D$ -time integrators, compared to the filtered results (figure 8), the spread between the various predictions is now more pronounced (e.g., 10FPM is only accurate to 4.45% up to  $k_{\text{Ny}}$ ). Nonetheless, the qualitative findings remain similar: BULLFROG outperforms the other  $D$ -time integrators for a fixed number of time steps. However, we note that the performance of FASTPDM could be slightly improved by initialising at a later time using 1BF or 2–3 LPT, rather than directly at  $a = 0$  (see below).

In figure 12 we compare our findings against COLA in the unfiltered case, using the same line styles and panel structure as in figure 9. We observe that the power spectrum of 100COLA closely approaches the reference result, except in the case when COLA is initialised at  $z_{\text{ini}} = 9$  – regardless of the  $n_{\text{LPT}}$  choice. This indicates that the 2LPT initialisation was pushed too far (if sub-percent accuracy is required), as the  $\geq 3$ LPT contributions missing in the initial conditions at  $z_{\text{ini}} = 9$  can never be recovered by the subsequent COLA integration, no matter the number of performed steps. 10COLA, however, performs well for all considered initialisation redshifts including specifically also  $z_{\text{ini}} = 9$ , provided that  $n_{\text{LPT}}$  is suitably adjusted. Overall, for the present experiments and considered scales, we find good performance with 10COLA for either  $n_{\text{LPT}} = 3.5$  and  $z_{\text{ini}} = 49$ , or for  $n_{\text{LPT}} = -2.5$  and  $z_{\text{ini}} = 9$ , resulting in sub-percent agreement with our reference result. The latter observation broadly aligns with the findings of ref. [69], though their reference result was obtained using a different gravity solver (Tree-PM using GADGET-2), whereas we apply an identical force calculation. We remark that

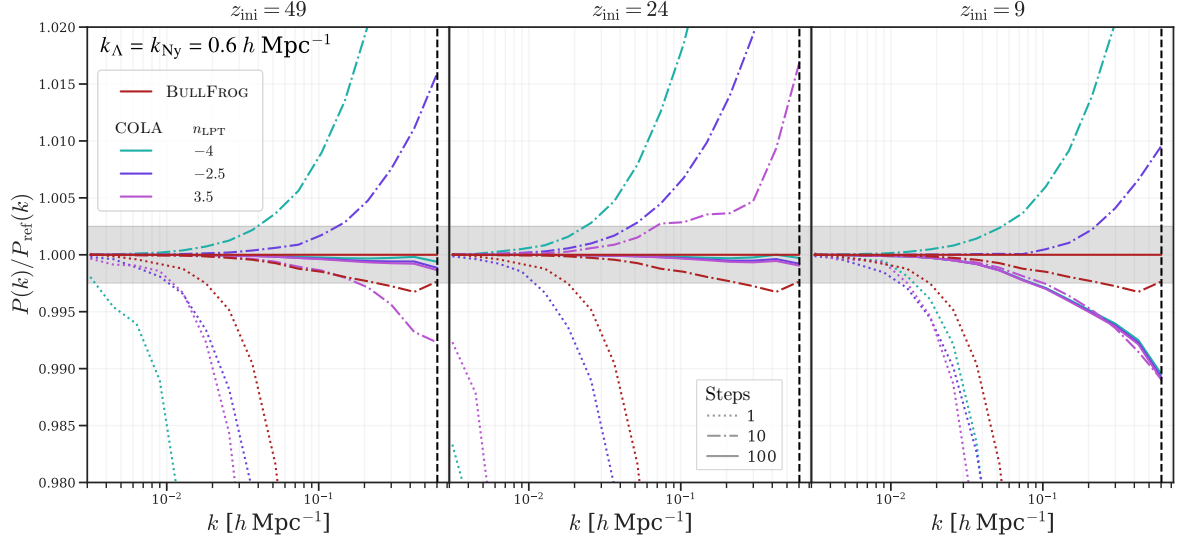


**Figure 12.** Similar as figure 9, but now for full  $\Lambda$ CDM simulations. For all three considered hyperparameters, 100COLA agrees with 100BF to better than 0.25%, however only if COLA is not initialised too late ( $z_{\text{ini}} \gtrsim 24$ ). For 10COLA, good performance is achieved either with  $n_{\text{LPT}} = 3.5$  at  $z_{\text{ini}} = 49$  or with  $n_{\text{LPT}} = -2.5$  at  $z_{\text{ini}} = 9$ , leading to sub-percent agreement with regards to the reference result.

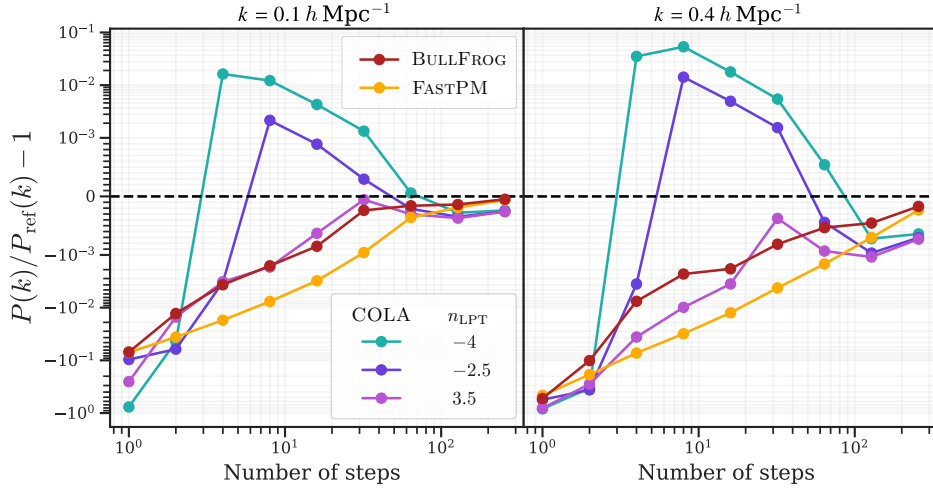


**Figure 13.** Convergence of the power spectrum for different integrators, plotted in a symmetric logarithmic scale, evaluated for two  $k$ -bins centred at  $k = 0.1 h \text{ Mpc}^{-1}$  (left) and  $k = 0.4 h \text{ Mpc}^{-1}$  (right) as a function of the number of time steps. We take 512BF as our base, and initialise all simulations at  $z_{\text{ini}} = 49$  using 2LPT, to ensure that all results converge towards the same solution for the number of steps  $n \rightarrow \infty$ .

it is likely that the COLA performance could be slightly improved for more refined choices of  $n_{\text{LPT}}$  paired with optimal choices of  $z_{\text{ini}}$  (see also below).<sup>4</sup> That said, we emphasise that also in this unfiltered  $\Lambda$ CDM case, 10BF achieves a smaller  $P(k)$  error than 10COLA with all parameter choices considered herein.

Finally, in figure 13 we compare the speed of convergence of the power-spectrum predictions

<sup>4</sup>See also the recent COCA approach that improves the 2LPT reference frame used in COLA by means of a field-level emulator [111].

for various fast integrators as a function of number of steps  $n$ , evaluated for two  $k$ -bins centred at  $k = 0.1 h \text{ Mpc}^{-1}$  (left panel) and  $k = 0.4 h \text{ Mpc}^{-1}$  (right panel). Here we take 512BF as our reference. Rather than initialising the  $D$ -time integrators at  $a = 0$  and COLA at some  $a > 0$  as above, we now initialise *all* simulations with 2LPT at  $z_{\text{ini}} = 49$  in this experiment. This is in order to ensure that the truncation errors at the time of initialisation are the same for all integrators, and hence the integrators should converge towards the same solution in the limit of infinitely many steps. Depending on the choice of the hyperparameter  $n_{\text{LPT}}$ , the COLA power spectrum overshoots already for a few steps, and the convergence behaviour is somewhat erratic. This observation suggests that the optimal value of  $n_{\text{LPT}}$  in the modified COLA scheme might benefit from a ‘lucky coincidence,’ where the overshooting of the power spectrum with a fairly low number of COLA steps compensates for the lack of power caused by the truncation errors due to the late initialisation with 2LPT. Indeed, for  $n_{\text{LPT}} = -2.5$ , for example, and the  $k$ -bins as shown in figure 13, very accurate COLA results are achieved for  $n \simeq 50$ , while some accuracy would be lost if  $n$  is, at first, just slightly increased (while ultimately converging towards the exact solution for  $n \gg 50$ ). Hence, the modified COLA scheme can end up in an ‘overdrive mode’ for certain tuples of  $(n_{\text{LPT}}, n)$ , where COLA is already very accurate, although the results are clearly not yet converged in  $n$ .

In contrast, figure 13 shows that both  $n\text{BF}$  and  $n\text{FPM}$  converge monotonically with  $n$ , while BULLFROG consistently achieves a significantly higher accuracy than FASTPM for any fixed  $1 < n \lesssim 256$ . For example, 32FPM [64FPM] reaches an accuracy of  $10^{-3}$  for the smaller [larger]  $k$ -bin relative to 512BF, while BULLFROG achieves this already with 16 [32] steps. For very few steps  $n \lesssim 10$ , the difference at  $k = 0.4 h \text{ Mpc}^{-1}$  is even more pronounced: sub-percent accuracy is achieved already with 4 BULLFROG steps, but only with  $> 16$  FASTPM steps. As a rough rule of thumb, applicable on the large scales considered, we find that BULLFROG is 2 – 3 times more efficient with respect to FASTPM for reaching a given target accuracy when ‘jump starting’ from  $z_{\text{ini}} = 49$  with 2LPT initial conditions. We emphasise that the BULLFROG-performance gain w.r.t. FASTPM comes virtually for free, as the only difference between these integrators is the different choice of weights (cf. eqs. 2.3 with eqs. 3.16). Nonetheless, the symplecticity of FASTPM can be expected to be beneficial when considering smaller scales (see discussion in section 3.2), for which reason we do not claim that BULLFROG makes FASTPM obsolete.

## 6 Conclusions

We introduce BULLFROG, the Blazingly fast, UV-complete, and LP<sub>T</sub>-informed LeaFroG integrator for cosmic structures. BULLFROG is 2LPT consistent without computing and storing 2LPT trajectories, unlike COLA. Instead, BULLFROG uses the first- and second-order  $\Lambda\text{CDM}$  growth functions as sole inputs, which are themselves solutions to ordinary differential equations (eqs. 3.5). Within a drift-kick-drift scheme, these growth functions appear in temporal coefficients within the kick update in a way, such that both the particle positions and momenta agree with the truncated 2LPT prediction, after each completed time step, before shell-crossing, and up to higher-order effects. See section 2 for a brief explanation how this is achieved, and appendix A for the kick-drift-kick variant of BULLFROG.

Crucially, BULLFROG is UV complete in the temporal sense and converges quadratically against the exact solution regardless of shell-crossing (section 4.3), but only if the actual growth functions are used and not approximations thereof (section 4.4). Also, as with any leapfrog integrator, we emphasise that second-order convergence is in general not achieved whenever the force field is not sufficiently regular [72], which in cosmology occurs at caustics [38].

In both spirit and implementation, BULLFROG can be viewed as the 2LPT extension of FASTPM [70], with the latter being consistent with the ZA (=1LPT). Furthermore, within the given

leapfrog scheme (see below), the difference between BULLFROG and FASTPM boils down to a choice of temporal coefficients, which are easily calculated in either case. Consequently, integrating BULLFROG into code environments that already support FASTPM is very straightforward.

BULLFROG heavily leverages the framework of  $D$ -time integrators (or ‘ $H$ -integrators’) introduced in refs. [72, 73], and makes slight improvements to their POWERFROG integrator, which is 2LPT consistent at the initial step, but only ZA consistent afterwards (section 3.2). Importantly, while there is a one-parameter family of ZA-consistent  $D$ -time integrators (which includes FASTPM and POWERFROG), BULLFROG is the unique 2LPT-consistent member of this class. This is because in BULLFROG the two degrees of freedom in the kick are used to exactly match the 1LPT and 2LPT terms. With no further degrees of freedom left, matching even higher LPT terms would require ‘sandwiching’ additional drifts and kicks within each step; we leave related avenues for future work.

The added benefit of BULLFROG in comparison to FASTPM is a two- to ten-fold reduction of time steps needed to reach a certain target accuracy in the matter power spectrum on mildly nonlinear scales (figs. 8, 11 and 13). Here, the reduction factor depends on the (large) scales considered, but also on the chosen initialisation time. Regarding the former, the performance gain of BULLFROG is most significant on mildly nonlinear scales ( $k \lesssim 0.6 h \text{ Mpc}^{-1}$ ), while the difference to FASTPM (and other  $D$ -time integrators) becomes negligible on highly nonlinear scales ( $5 h \text{ Mpc}^{-1} \lesssim k \lesssim 30 h \text{ Mpc}^{-1}$ ), since 2LPT consistency barely matters in that regime. Nonetheless, it is worth highlighting that all  $D$ -time integrators that are at least ZA consistent significantly outperform the standard symplectic leapfrog integrator, even on these highly nonlinear scales, as demonstrated in figure 10 of ref. [72].

All considered  $D$ -time integrators (in DKD form) support the start of simulations directly at time zero, but there, FASTPM performs the weakest due to the missing 2LPT consistency. In all our LSS experiments, the performance of BULLFROG is best among the  $D$ -time integrators, followed closely by POWERFROG, and not so closely by FASTPM. Nonetheless, FASTPM is the only  $D$ -time integrator that is symplectic [72], which is a desired property for modelling virialised systems such as halos.

We also carried out tests against COLA, which is not a  $D$ -time integrator, but incorporates 2LPT by performing a coordinate boost onto the explicitly computed 2LPT trajectories at the level of a standard leapfrog stepper [68]. We confirm previous findings in the literature that COLA can achieve fast and accurate predictions for the LSS, which however sensitively depend on the choice of the  $n_{\text{LPT}}$  hyperparameter<sup>3</sup> that appears within their modified scheme. BULLFROG, by contrast, has no free parameter – other than the number of time steps and their spacing – and has a slightly smaller computational footprint than COLA, as 2LPT consistency comes virtually at no extra cost.

From the perspective of perturbation theory, and before shell-crossing, BULLFROG amounts to implementing a multi-step LPT scheme within an  $N$ -body simulation. The ‘tasks’ of the  $N$ -body integrator can be consistently analysed throughout in Lagrangian space, i.e., without the need for swapping temporarily back to Eulerian coordinates for determining the force field on a regular grid (section 4). The swapping between Lagrangian (i.e., comoving with particles) and Eulerian (fixed) coordinates leads to advection terms, but through a careful analysis we find that these effects are actually accommodated for, at least up to second-order in perturbation theory; see appendix B for complementary perturbative considerations in semi-Lagrangian form that mimic these swapping effects. After shell-crossing, when some or many particles are not single stream anymore, BULLFROG trajectories start deviating from those predicted by LPT, since BULLFROG accounts for multi-streaming in the force computation, while LPT does not. In fact, this departure from perturbative trajectories is essential for BULLFROG to converge toward the correct solution, regardless of shell-crossing.

We also compared BULLFROG against LPT, which is known to provide accurate results as long as most particles remain in the single-stream regime [33–36]. For  $\Lambda$ CDM simulations with a low UV cutoff ( $k_{\Lambda} = 0.1 h \text{ Mpc}^{-1}$ ), where essentially all particles are still single stream down to  $z = 0$

(figure 7), we find very good agreement between BULLFROG and LPT. However, achieving comparable accuracy with LPT requires high-order solutions, which become prohibitive in terms of memory and computational time due to the need for de-aliasing and storing the rapidly increasing number of perturbation kernels with increasing order. Even worse, for less strong filtering ( $k_\Lambda = 0.2 h \text{ Mpc}^{-1}$ ), we observe already the first signatures of loss of LPT convergence at  $z = 0$ , owing to the fact that many particles have left the single-stream regime. BULLFROG and the other  $D$ -time integrators, by contrast, have a constant memory footprint when increasing the number of time steps.

From a practical standpoint, BULLFROG is an easy-to-implement, fast, and accurate forward model, and we imagine it to be useful in a host of cosmological applications. Indeed, we have seen that BULLFROG converges *monotonically* towards the exact solution when increasing the number of time steps, with the residue being pushed to smaller / nonlinear scales. This means that with BULLFROG, one simply needs to adjust the (low) number of time steps required to achieve a desired accuracy at a given scale. Moreover, BULLFROG could replace LPT as a superior forward model in many applications, such as within effective-fluid descriptions, data inference, machine-learning tasks, or hybrid approaches thereof (e.g. refs. [78, 80, 98, 112–115]).

Let us comment on possible future extensions of BULLFROG. The current implementation assumes a spatially flat  $\Lambda$ CDM Universe with a cosmological constant. Relaxing the flatness assumption or allowing for a time-evolving dark-energy background component is feasible, likely by simply updating the linear growth rate within the  $D$ -time integrator as done by the FASTPM-based approach of Ref. [65], supplemented with revisiting the second-order matching conditions against analytical LPT solutions. Similar techniques could also be applied to allow for non-zero neutrino masses in BULLFROG. Also here, an integrator with a refined time variable is expected to be highly beneficial (see ref. [71] for a FASTPM-based approach). However, owing to the scale-dependent nature of the multi-fluid problem at hand, it is likely that further alterations would be necessary, such as modifications to the source term in the Poisson equation; see e.g. refs. [76, 116–118] for potentially fruitful starting points. Finally, redshift-space distortions and lightcone effects could be incorporated directly at the level of the integrator, which would further assist in bridging the gap between the theoretical modelling and observational data; we leave related implementations to future work.

## Acknowledgments

We thank Giovanni Cabass, Stéphane Colombi, Fabian Schmidt, Jens Stücker, Zvonimir Vlah, and Yvonne Y.Y. Wong for related discussions and/or comments on the manuscript. A differentiable implementation of BULLFROG using JAX, on which the results in this work are based, will be made publicly available in the near future as part of the DISCO-DJ framework (see ref. [119] for the differentiable Einstein–Boltzmann solver). Furthermore, a particle-mesh code implementing BULLFROG into the MPI-parallel  $n$ LPT IC generator MONOFONIC is available upon request.

## A KDK version of BULLFROG (BF-KDK)

In section 4 we have determined the BULLFROG-weights based on a DKD scheme. Here we consider BULLFROG within a KDK scheme, with updates from step  $n \rightarrow n + 1$  according to

$$\mathbf{v}_{n+1/2} = \mathbf{a} \mathbf{v}_n + \mathbf{b} D_n^{-1} \mathbf{A}(\mathbf{x}_n), \quad (\text{A.1a})$$

$$\mathbf{x}_{n+1} = \mathbf{x}_n + \Delta D \mathbf{v}_{n+1/2}, \quad (\text{A.1b})$$

$$\mathbf{v}_{n+1} = \bar{\mathbf{a}} \mathbf{v}_{n+1/2} + \bar{\mathbf{b}} D_{n+1}^{-1} \mathbf{A}(\mathbf{x}_{n+1}). \quad (\text{A.1c})$$

Here,  $\nabla_x \cdot \mathbf{A} = -\delta$  as before, while  $\mathbf{a}, \mathbf{b}, \bar{\mathbf{a}}$  and  $\bar{\mathbf{b}}$  are weights that we determine in the following appendix, such that the integrator is 2LPT consistent. In appendix A.2, we then verify that the resulting integrator is second-order accurate.

We will see that the BF-KDK has some disadvantage for initialising simulations at  $D = 0$  as opposed to its DKD variant (which in the main text we often abbreviate just with BF), for which reason we do not recommend using its KDK version for that purpose. However, the KDK variant has a conceptual advantage at later time steps: For BF-KDK, the acceleration  $\mathbf{A}$  is always evaluated at integer time steps – as opposed to the DKD variant where  $\mathbf{A}$  is evaluated at the half step. Thus, provided that the 2LPT matching condition is incorporated at integer time steps,  $\mathbf{A}$  is by construction exactly evaluated at the truncated 2LPT positions in the KDK case. By contrast, in the DKD scheme and for finite  $\Delta D$ ,  $\mathbf{A}$  is *never* exactly evaluated at the truncated 2LPT position due to temporal discretisation (see figure 3), which then needs to be rectified by choosing appropriate weights to autocorrect for this slight misplacement. Moreover, KDK integrators are favourable when using individual time steps [120], which are routinely implemented in industry-standard codes. Thus, extending these codes with BULLFROG might be more straightforward and give rise to interesting extensions of the present work, such as the development of hybrid schemes that follow BULLFROG at early times / on large scales and employ a symplectic scheme at late times / on small scales.

### A.1 Determining the weights

Similarly as discussed in section 4.1, BULLFROG could be initialised at  $D = 0$  when formulated in KDK form, however we choose not to, for the following reason: if we start at  $n = 0$  and employ the initial conditions (3.19), the acceleration field  $\mathbf{A}(\mathbf{x}_0)$  within the first kick step would be exactly zero; as a direct consequence,  $\mathbf{v}_{1/2}$  and the following drift update  $\mathbf{x}_1$  could only be set to agree with ZA motion at fixed truncation order. Thus, initialising BF-KDK at  $D = 0$  is tantamount to starting on the Zel'dovich trajectory at the end of the first time step  $\Delta D$ . While the weights appearing in the second kick update could then be adjusted to agree with the 2LPT velocity at fixed truncation order, we would be left with a somewhat imbalanced situation since the positions would be lagging one order behind in terms of LPT. This imbalance could be rectified in subsequent time steps, such that the KDK integrator initialised at  $D = 0$  matches both the truncated 2LPT positions and velocities at later times steps (namely from  $n = 2$  onwards), however this would require individually designed weights for the first few time steps, which we choose to avoid for the sake of simplicity.

Therefore, in what follows we consider exclusively the case  $n \geq 1$  and thus assume that the particle positions and velocities are 2LPT consistent after the first completed time step, i.e., the matching conditions are ( $n \geq 1$ )

$$\mathbf{x}_n \stackrel{!}{=} \mathbf{x}^{2\text{LPT}}|_{D=D_n} + h.o.t., \quad \mathbf{v}_n \stackrel{!}{=} \mathbf{v}^{2\text{LPT}}|_{D=D_n} + h.o.t., \quad (\text{A.2})$$

where the 2LPT solutions are listed in eqs. (3.5). Of course, the required initialisation process for this could be done in various ways, specifically by using a single BULLFROG step in DKD form (eqs. 2.1 for  $n = 0$ ), or simply by initialising the system using a standard 2LPT initial condition generator (see e.g. refs. [17, 83]).

To determine the weights, we first observe that within the KDK scheme, the acceleration field is always evaluated at the temporal boundaries of the step. Imposing our matching 2LPT conditions (A.2) thus allows us to estimate  $\mathbf{A}$  perturbatively by directly applying the perturbative considerations from section 3.1. Specifically, evaluating the truncated 2LPT acceleration (3.13) at  $D = D_n$  and using the matching conditions (A.2) in the first kick and drift updates, it is straightforward to derive

$$\mathbf{v}_{n+1/2} = -\nabla_q \varphi + \frac{E_{n+1} - E_n}{\Delta D} \nabla_q^{-1} \mu_2 + h.o.t., \quad (\text{A.3})$$



which implies the following form for the first pair of weights,

$$\boxed{\alpha = \frac{D_n(E_{n+1} - E_n) + \Delta D(D_n^2 - E_n)}{\Delta D(D_n^2 + E_n D_n - E_n)} \stackrel{\text{EdS}}{\asymp} 1 - \frac{3}{4\mathfrak{n}}, \quad \mathfrak{b} = 1 - \alpha \stackrel{\text{EdS}}{\asymp} \frac{3}{4\mathfrak{n}},} \quad (\text{A.4a})$$

where we remind the reader that  $\mathfrak{n} = a_n/\Delta a$  (which is equal to  $n$  for uniform time steps). Similarly, using eq.(A.3) as well as the 2LPT matching conditions and plugging them in the last kick update (A.1c), we obtain for the second pair of weights

$$\boxed{\bar{\alpha} = \Delta D \frac{D_{n+1}^2 + D_{n+1}E'_{n+1} - E_{n+1}}{D_{n+1}(E_{n+1} - E_n) + \Delta D(D_{n+1}^2 - E_{n+1})} \stackrel{\text{EdS}}{\asymp} \frac{4 + 4\mathfrak{n}}{7 + 4\mathfrak{n}}, \quad \bar{\mathfrak{b}} = 1 - \bar{\alpha} \stackrel{\text{EdS}}{\asymp} \frac{3}{7 + 4\mathfrak{n}},} \quad (\text{A.4b})$$

which concludes the derivation. Equations (A.4) are the weights for the KDK version of BULLFROG, to be used as sole inputs in equations (A.1).

For completeness, we mention that in the EdS case, the BF-KDK is remarkably similar to the  $D$ -time integrator ‘LPTFROG’ introduced by ref. [72], with the only difference that with BULLFROG the velocity in the friction term (see their eqs. I.6) is evaluated at the interval *boundaries*  $D_n$  and  $D_{n+1}$  in the first and second kick half, respectively, instead of the interval midpoint as for LPTFROG. As discussed in that reference, LPTFROG can be viewed as a slight generalisation of the leapfrog method discussed in [121, Example 2] to the cosmological case. That method, in turn, is derived from the same discrete Euler–Lagrange equation that also forms the basis of ‘contact integrators’, which respect the contact structure of the underlying system. Consequently, the same connection to contact geometry also exists for BULLFROG, and while a rigorous analysis in this direction is beyond the scope of this work, it is remarkable that building 2LPT into an integrator leads to a method that could also have been obtained by approaching the Vlasov–Poisson system from a contact-geometrical perspective.

## A.2 Numerical convergence

To validate that BF-KDK is globally second-order accurate as  $\Delta D \rightarrow 0$ , we need to establish two distinct findings, namely that

- ①  $\alpha$  and  $\bar{\alpha}$  are separately first-order accurate, and that
- ② the combination  $\alpha\bar{\alpha} =: \alpha_{\text{eff}}$  is second-order accurate.

Since the remaining two coefficients  $\mathfrak{b}$  and  $\bar{\mathfrak{b}}$  in the kick are defined via the Zel’dovich consistency conditions  $\mathfrak{b} = 1 - \alpha$  and  $\bar{\mathfrak{b}} = 1 - \bar{\alpha}$ , these conditions on  $\alpha$  and  $\bar{\alpha}$  are sufficient for obtaining a second-order scheme, similar to [72, Proposition 6]. The first condition is strictly necessary to ensure global second-order accuracy; indeed it is easy to construct integrator weights that violate ① but satisfy ②, which however would imply a drift with an inconsistent velocity, spoiling second-order accuracy.

To demonstrate that both conditions are separately satisfied, we expand the BULLFROG weights in powers of  $\Delta D$  and compare the resulting coefficients with the reference values from a second-order accurate KDK integrator. For the latter, we take the weights for the KDK version of FASTPM,<sup>2</sup> which read [72]  $\alpha^{\text{FPM}} = \mathcal{F}_n/\mathcal{F}_{n+1/2}$  and  $\bar{\alpha}^{\text{FPM}} = \mathcal{F}_{n+1/2}/\mathcal{F}_{n+1}$  such that  $\alpha^{\text{FPM}} = \alpha^{\text{FPM}}\bar{\alpha}^{\text{FPM}}$  as before (see section 4.3).

We begin by verifying the condition  $\textcircled{1}$  for which we expand the reference values as

$$\alpha^{\text{FPM}} = 1 - \alpha_1^{\text{FPM}} \Delta D + O(\Delta D^2), \quad \bar{\alpha}^{\text{FPM}} = 1 - \bar{\alpha}_1^{\text{FPM}} \Delta D + O(\Delta D^2), \quad (\text{A.5})$$

where

$$\alpha_1^{\text{FPM}} = \bar{\alpha}_1^{\text{FPM}} = \frac{\mathcal{F}'}{2\mathcal{F}} = \frac{3aD}{4\mathcal{F}^2}, \quad (\text{A.6})$$

which is precisely equal to  $\alpha_1^{\text{BF}}/2$  (cf. eq. 4.16); here and in the following, functional dependencies are w.r.t.  $D = D_n$  which we omit for notational simplicity. We compare the coefficients (A.5) against those of BULLFROG, which are

$$\alpha = 1 - \alpha_1 \Delta D + O(\Delta D^2), \quad \bar{\alpha} = 1 - \bar{\alpha}_1 \Delta D + O(\Delta D^2), \quad (\text{A.7})$$

with

$$\alpha_1 = \bar{\alpha}_1 = [1/2] D E'' W^{-1}, \quad (\text{A.8})$$

where  $W = E - D(D + E')$ . Equation (A.8) is equal to  $\alpha_1^{\text{BF}}/2$  (cf. eq. 4.18) and thus, by virtue of identical derivations as carried out in section 4.3, we conclude that the BULLFROG weights are locally first-order accurate, as required by condition  $\textcircled{1}$ .

Secondly and finally, to verify that condition  $\textcircled{2}$  is met, we consider the second-order expansion of the reference value  $\alpha^{\text{FPM}} = \alpha^{\text{FPM}} \bar{\alpha}^{\text{FPM}}$ , which we repeat here for convenience,

$$\alpha^{\text{FPM}} = 1 - \alpha_1^{\text{FPM}} \Delta D + \alpha_2^{\text{FPM}} \Delta D^2 + O(\Delta D^3), \quad (\text{A.9})$$

where

$$\alpha_1^{\text{FPM}} = \frac{\mathcal{F}'}{\mathcal{F}}, \quad \alpha_2^{\text{FPM}} = \frac{2\mathcal{F}'^2 - \mathcal{F}\mathcal{F}''}{2\mathcal{F}^2}. \quad (\text{A.10})$$

By contrast, expanding the effective BULLFROG weight  $\alpha_{\text{eff}} = \alpha \bar{\alpha}$  to second order in the  $\Delta D$  expansion, we have

$$\alpha_{\text{eff}} = 1 - \alpha_{1,\text{eff}} \Delta D + \alpha_{2,\text{eff}} \Delta D^2 + O(\Delta D^3), \quad (\text{A.11})$$

where

$$\alpha_{1,\text{eff}} = D E'' W^{-1}, \quad \alpha_{2,\text{eff}} = -[1/2] (D E''' + E'') W^{-1} - D^2 E'' W^{-2}. \quad (\text{A.12})$$

Actually, these two  $\Delta D$ -coefficients coincide exactly with those as derived in the DKD case of BULLFROG (cf. eq. 4.18); thus, we conclude that also BF-KDK is second-order accurate.  $\blacksquare$

## B Multi-time LPT and $N$ -body simulations

In the main text, we have determined the acceleration  $\mathbf{A}$  appearing in the kick step of BULLFROG by a perturbative calculation that was performed strictly in Lagrangian coordinates (section 4). The reader might be surprised how this is possible or even justified, especially considering that cosmological  $N$ -body simulations employ a ‘semi-Lagrangian scheme’ (elucidated below), and thus, such simulations are not strictly Lagrangian.

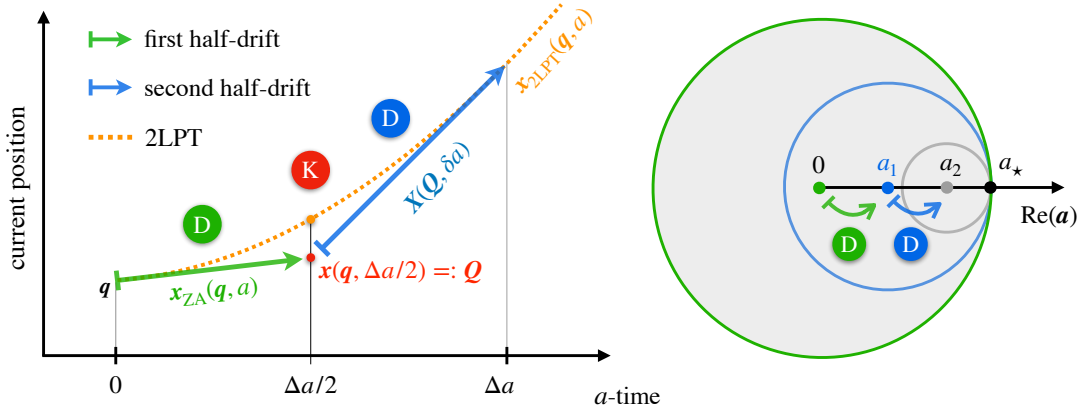


**Figure 14.** *Left sketch:* First DKD step of BULLFROG (green and blue arrows), as compared against the truncated 2LPT solution (orange dashed) in an EdS universe. In BULLFROG, the first drift is executed within the ZA, therefore, particles will be at a misplaced position at the half-time  $a = \Delta a/2$  w.r.t. 2LPT. To determine the resulting acceleration at half time, we employ time-shifted LPT (TSLPT, appendix B.1), which allows us to initialise the second drift (blue arrow) with the density and velocity inputted from the previous drift (green arrow), expressed in ‘fresh’ Lagrangian coordinates denoted  $\mathbf{Q} := \mathbf{x}(\mathbf{q}, \Delta a/2)$ , and current position  $\mathbf{X}(\mathbf{Q}, \delta a)$ , where here  $\delta a = a - \Delta a/2$ . Evaluating then  $\mathbf{X}(\mathbf{Q}, \delta a)$  at  $\delta a \rightarrow 0^+$  allows us to determine the acceleration at half time (appendix B.2). This strategy closely resembles the semi-Lagrangian nature inherent in the first DKD step of BULLFROG. *Right sketch:* Shown are various discs of convergence of displacement power series in the formally complexified  $a$ -time variable, denoted with  $\mathbf{a}$  in the following. Specifically, the grey disc indicates the disc of convergence of standard LPT which is limited by a mathematical singularity located at complex time  $\mathbf{a} = \mathbf{a}_*$  (which generically arises after shell-crossing [35, 36]). The blue circle centred at  $\mathbf{a} = \mathbf{a}_1$  denotes the convergence radius of TSLPT at that time step; and so on. The outlined strategy invokes a generalisation of the analytic continuation theorem of Weierstrass, which in the present case amounts to displacing particles within a multi-time stepping approach.

While there are many different implementations of semi-Lagrangian schemes in the literature, let us explain in words how such a scheme can be viewed in light of DKD integrators:

$N$ -body particles are displaced in Lagrangian coordinates. To determine the resulting gravitational acceleration from this displacement, one temporarily swaps to a Eulerian reference frame to solve the Poisson equation  $\nabla_{\mathbf{x}} \cdot \mathbf{A} = -\delta$ . This swapping from Lagrangian to Eulerian space is achieved using interpolation methods; most common is the use of the cloud-in-cell interpolation, but there are of course many other methods (see e.g. [16] for a recent review). Once the Poisson equation is solved, one again uses an interpolation scheme, thereby swapping back to Lagrangian coordinates where the resulting acceleration  $\mathbf{A}$  is assigned to the  $N$ -body particles. One then updates their velocity during the kick and advances them in the second half drift, all in Lagrangian space, completing the DKD operation. (All this is repeated for consecutive time steps.)

In the subsequent sections, we analyse the aforementioned semi-Lagrangian method by analytical means. For this we introduce a time-shifted variant of LPT, which comes with the crucial addition that temporal expansions are performed not around  $a = 0$  but any  $a_s > 0$ . Here and in the following, we work with an EdS cosmology for simplicity, but this could be straightforwardly rectified, for which we give explicit instructions when appropriate.

In the following, we introduce the time-shifted equations of motion together with a time-shifted LPT expansion, which we dub TSLPT. In appendix B.2, we apply the TSLPT to the calculation of the force during the initial step of BULLFROG. See figure 14 where we show an illustration of our strategy to compute the force at the first half step (left panel), as well as the mathematical idea of TSLPT to

drift particles within a multi-step setup (right panel).

### B.1 Time-Shifted Lagrangian Perturbation Theory

Let us begin with the basic equations that are at the core of standard (i.e., non-shifted) LPT, given here for an EdS universe for simplicity,

$$\frac{2}{3}a^2\mathbf{x}''(\mathbf{q}, a) + a\mathbf{x}'(\mathbf{q}, a) = -\nabla_{\mathbf{x}}\phi, \quad \delta(\mathbf{q}, a) = \frac{1}{J} - 1, \quad \nabla_{\mathbf{x}}^2\phi(\mathbf{q}, a) = \delta(\mathbf{q}, a), \quad (\text{B.1})$$

where from here on, temporal derivatives are w.r.t. the scale-factor time  $a$  and denoted with a prime. In standard LPT, these equations are solved with  $\mathbf{x} - \mathbf{q} = \boldsymbol{\psi} = \sum_{n=1}^{\infty} \boldsymbol{\psi}^{(n)} a^n$ , i.e., a power series expansion about  $a = 0$ ; see eqs. (3.5) for the (well-known) EdS results up to second order in the limit  $\Lambda \rightarrow 0$ . We remark that, beyond second order, one needs to solve for the zero-vorticity constraint (the Cauchy invariants) in order to incorporate transverse displacements; see, e.g., [15].

By contrast, with TSLPT we aim to enable perturbative expansions about a shifted expansion point  $a_s \geq 0$ , which we take to be a constant and  $s$  is an integer counter. Here,  $a_s$  can be arbitrarily large and thus is not a perturbative quantity. To accommodate the necessary framework for TSLPT, we proceed twofold. First, we define a ‘fresh’ Lagrangian map  $\mathbf{Q} \mapsto \mathbf{X}(\mathbf{Q}, \delta a)$  from a ‘fresh initial time’  $\delta a = 0$  to evolved time  $\delta a$  (our expansion parameter), where  $a = a_s + \delta a$  (see left panel in figure 14 for  $a_s = \Delta a/2$ ). Second, we shift eqs. (B.1) according to  $a \rightarrow a_s + \delta a$ . The resulting ‘time-shifted’ equations of motion are then

$$\frac{2}{3}(a_s + \delta a)^2 \mathbf{X}''(\mathbf{Q}, \delta a) + (a_s + \delta a) \mathbf{X}'(\mathbf{Q}, \delta a) = -\nabla_{\mathbf{X}}\phi(\mathbf{Q}, \delta a), \quad (\text{B.2a})$$

$$\delta(\mathbf{Q}, \delta a) = \frac{1 + \delta_s(\mathbf{Q})}{J(\mathbf{Q}, \delta a)} - 1, \quad (\text{B.2b})$$

$$\nabla_{\mathbf{X}}^2\phi(\mathbf{Q}, \delta a) = \delta(\mathbf{Q}, \delta a), \quad (\text{B.2c})$$

where, importantly, we have added in eq. (B.2b) the ‘initial’ density  $\delta_s := \delta(\delta a = 0)$  provided at  $a = a_s$ , which is in general nonzero (as opposed to eq. B.1 where initial quasi-homogeneity is assumed). We remark that, as in the standard LPT case, one also needs to solve for the zero-vorticity constraint  $\nabla_{\mathbf{x}} \times \mathbf{v} = \mathbf{0}$ , which in Lagrangian coordinates becomes  $\varepsilon_{ijk} X_{i,j} X'_{l,k} = 0$  for the shifted map. For our initial conditions, however, the resulting transverse displacement contributions only become nonzero beyond the second order, therefore we do not consider this constraint in the following.

To solve the shifted equations (B.2), we define the ‘shifted’ displacement  $\mathbf{S} = \mathbf{X} - \mathbf{Q}$ , for which we impose the Ansatz

$$\mathbf{S}(\mathbf{Q}, \delta a) = \sum_{n=1}^{\infty} \mathbf{S}^{(n)}(\mathbf{Q}) \delta a^n. \quad (\text{B.3})$$

The first-order solution follows directly from the definition of the shifted map or, put differently, from momentum conservation evaluated at  $\delta a = 0$ , i.e.,  $\mathbf{S}'(\mathbf{Q}, \delta a)|_{\delta a=0} = \mathbf{S}^{(1)}(\mathbf{Q}) = \mathbf{v}_s(\mathbf{Q})$ , where  $\mathbf{v}_s := \mathbf{v}(\delta a = 0)$  is the velocity at time  $a = a_s$ . The first-order solution is then used as an input to solve the evolution equations at second order. Note that in TSLPT, a second-order treatment is the absolute minimum, otherwise the second input field  $\delta_s(\mathbf{Q})$  is not passed over, thereby violating the second-order structure of the underlying differential equation. In summary, we find for the first and second-order solutions respectively

$$S_{l,l}^{(1)}(\mathbf{Q}) = \nabla_{\mathbf{Q}} \cdot \mathbf{v}_s = -\varphi_{,ll}^{\text{ini}}(\mathbf{Q}) - \frac{\Delta a}{2} \left( \varphi_{,lm}^{\text{ini}} \varphi_{,lm}^{\text{ini}} + \varphi_{,l}^{\text{ini}} \varphi_{,lmm}^{\text{ini}} \right), \quad (\text{B.4a})$$

$$S_{l,l}^{(2)}(\mathbf{Q}) = -\frac{3}{4a_s} \left[ \frac{\delta_s(\mathbf{Q})}{a_s} + S_{l,l}^{(1)}(\mathbf{Q}) \right] = -\frac{3}{4} \mu_2(\mathbf{Q}). \quad (\text{B.4b})$$

In summary, the time-shifted displacement truncated at second order is then

$$S(\mathbf{Q}, \delta a) = -\delta a \nabla_{\mathbf{Q}} \varphi^{\text{ini}}(\mathbf{Q}) - \delta a a_s \nabla_{\mathbf{Q}}^{-1} \left( \varphi_{,lm}^{\text{ini}} \varphi_{,lm}^{\text{ini}} + \varphi_{,l}^{\text{ini}} \varphi_{,lmm}^{\text{ini}} \right) - \frac{3}{4} \delta a^2 \nabla_{\mathbf{Q}}^{-1} \mu_2 + O(\delta a^3), \quad (\text{B.5})$$

where  $\nabla_{\mathbf{Q}}^{-1} := \nabla_{\mathbf{Q}}^{-2} \nabla_{\mathbf{Q}}$ . Next, as promised, we briefly outline the steps needed to generalise TSLPT to a  $\Lambda$ CDM cosmology. A potentially good starting point for this is the equations of motion formulated in  $D$ -time, which are given in ref. [97, eqs. 5-7]. These equations can be shifted according to  $D \rightarrow D_1 + \Delta D$  and solved by an Ansatz for  $S$  in powers of  $\Delta D$ , which is a straightforward exercise. However, the shifted displacement results should be resummed, so as to include all  $\Lambda$  terms proportional to the given spatial terms to fixed order in perturbation theory; see ref. [97, Secs. 4.1-4.2] where this has been done for the nonshifted LPT case. We leave related avenues for TSLPT for future work.

Before concluding this appendix, let us outline a (delayed) motivation and underlying strategy for TSLPT; see the right panel of figure 14 for a related illustration. Mathematically speaking, one does not need TSLPT to begin with, since LPT converges until the time of first shell-crossing and slightly beyond [33–36]: Lagrangian perturbation theory, which employs effectively a time-Taylor series, is not limited by complex-in- $a$ -time singularities, but by a mathematical singularity located on the real-time axis. For generic initial conditions, this ‘real singularity’ occurs after shell-crossing, implying that LPT is time-analytic and thus converges for the whole real-time branch from initial time, and at least until shell-crossing. However, evaluating the LPT displacement at times close to its final time of convergence requires large orders in order to get sufficiently accurate representations for the displacement (except in 1D where ZA is the only nonzero term in the Taylor series). In practice, generating LPT solutions at large orders is computationally prohibitive (see main text).

Time-shifted LPT avoids this computational drawback, by replacing a mega-time step in LPT with consecutive TSLPT steps: since by definition the TSLPT steps will be smaller, a lower-order truncation of the shifted displacement should remain accurate, basically since the fresh input fields are assigned at each new time step. The underlying mathematical idea is rooted in a generalisation of the Weierstrass analytic continuation theorem for analytic functions; see ref. [122] for numerical implementations of highly related schemes, however applied to incompressible Euler flow.

## B.2 $N$ -body force computation in light of time-shifted LPT

Finally, let us proceed with the main task of this appendix, which is illustrated in the left panel of figure 14: Given the LPT density and velocity at the evolved position  $a = \Delta a/2$ , we seek to employ TSLPT to determine the acceleration field at that half step. The result is identical to the one outlined in the main text, but the involved technical procedure is certainly very different. The present complementary derivation serves two main purposes, namely (1) to validate TSLPT, (2) and as a consistency check for the acceleration computation in the main text.

To achieve this, and to closely resemble the initialisation process of BULLFROG (and for any  $D$ -time integrator as well), we assume here that the first drift operation has been executed assuming Zel’dovich dynamics (see section 3.2 and in particular eq. 3.19); this restriction can easily be alleviated if needed. For the first half drift at  $a = 0$ , we can employ just standard LPT, which implies

$$\mathbf{x}(\mathbf{q}, \Delta a/2) = \mathbf{q} - \frac{\Delta a}{2} \nabla_{\mathbf{q}} \varphi^{\text{ini}}, \quad \text{D} \quad (\text{B.6})$$

which allows us to determine the density and velocity at the half-time,

$$\begin{aligned}\delta(\mathbf{x}(\mathbf{q}, \Delta a/2)) &= \frac{1}{\det[\delta_{ij} - (\Delta a/2)\varphi_{,ij}^{\text{ini}}]} - 1 \\ &= \frac{\Delta a}{2}\varphi_{,ll}^{\text{ini}}(\mathbf{q}) - \left(\frac{\Delta a}{2}\right)^2 \mu_2 + \left(\frac{\Delta a}{2}\right)^2 \varphi_{,ll}^{\text{ini}}\varphi_{,mm}^{\text{ini}} + h.o.t. =: \delta_{1/2}(\mathbf{q}),\end{aligned}\quad (\text{B.7})$$

$$\mathbf{v}(\mathbf{x}(\mathbf{q}, \Delta a/2)) = -\nabla_{\mathbf{q}}\varphi^{\text{ini}}(\mathbf{q}) =: \mathbf{v}_{1/2}(\mathbf{q}), \quad (\text{B.8})$$

where quantities related to the first [second] drift half are coloured in green [blue]. Before employing TSLPT, we need to make sure that the fields for the second drift half are passed over by taking the fresh coordinates into account. Since we only consider results to second-order accuracy, that task is achieved by synchronising the coordinates at  $a = \Delta a/2$  with

$$\mathbf{q} - \frac{\Delta a}{2}\nabla_{\mathbf{q}}\varphi^{\text{ini}}(\mathbf{q}) =: \mathbf{Q} \quad \Rightarrow \quad \mathbf{q} = \mathbf{Q} + \frac{\Delta a}{2}\nabla_{\mathbf{Q}}\varphi^{\text{ini}}(\mathbf{Q}) + h.o.t., \quad (\text{B.9})$$

Plugging the second expression into the evolved fields (B.7)–(B.8), one then gets the input fields as a function of the fresh coordinates,

$$\begin{aligned}\delta_{1/2}(\mathbf{Q}) &= \frac{\Delta a}{2}\varphi_{,ll}^{\text{ini}}(\mathbf{Q}) + \left(\frac{\Delta a}{2}\right)^2 \varphi_{,l}^{\text{ini}}\varphi_{,lmm}^{\text{ini}} - \left(\frac{\Delta a}{2}\right)^2 \mu_2 + \left(\frac{\Delta a}{2}\right)^2 \varphi_{,ll}^{\text{ini}}\varphi_{,mm}^{\text{ini}} + h.o.t., \\ \mathbf{v}_{1/2}(\mathbf{Q}) &= -\nabla_{\mathbf{Q}}\varphi^{\text{ini}}(\mathbf{Q}) - \frac{\Delta a}{2}\varphi_{,l}^{\text{ini}}\nabla_{\mathbf{Q}}\varphi_{,l}^{\text{ini}} + h.o.t.\end{aligned}\quad (\text{B.10})$$

Plugging the input fields (B.10) in the TSLPT results (B.4) while setting  $a_s = \Delta a/2$  leads directly to the time-shifted displacement

$$\mathbf{S}(\mathbf{Q}, \delta a) = -\delta a \nabla_{\mathbf{Q}}\varphi^{\text{ini}}(\mathbf{Q}) - \delta a \frac{\Delta a}{2}\nabla_{\mathbf{Q}}^{-1} \left( \varphi_{,lm}^{\text{ini}}\varphi_{,lm}^{\text{ini}} + \varphi_{,l}^{\text{ini}}\varphi_{,lmm}^{\text{ini}} \right) - \frac{3}{4}\delta a^2\nabla_{\mathbf{Q}}^{-1}\mu_2, \quad \text{D} \quad (\text{B.11})$$

truncated up to second order. Equipped with the shifted displacement, we can determine the acceleration at the half step in three simple steps. First, similar as in the main text, we exploit the equivalence principle and express the gravitational field, here defined with  $\mathbf{A} = -\nabla_x\phi$ , in terms of the acceleration:

$$\frac{2}{3}(\Delta a/2 + \delta a)^2 \mathbf{X}'' + (\Delta a/2 + \delta a) \mathbf{X}' = \mathbf{A} \quad (\text{B.12})$$

(eq. (B.2a) for  $a_s = \Delta a/2$ ). Second, we replace  $\mathbf{X} = \mathbf{Q} + \mathbf{S}$  and use eq. (B.11); evaluating eq. (B.12) then at  $\delta a \rightarrow 0^+$  leads to the acceleration at the half step,

$$\mathbf{A}(\mathbf{Q}, \delta a = 0) = -\frac{\Delta a}{2}\nabla_{\mathbf{Q}}\varphi^{\text{ini}}(\mathbf{Q}) - \left(\frac{\Delta a}{2}\right)^2 \nabla_{\mathbf{Q}}^{-1} \left[ \mu_2 + \varphi_{,lm}^{\text{ini}}\varphi_{,lm}^{\text{ini}} + \varphi_{,l}^{\text{ini}}\varphi_{,lmm}^{\text{ini}} \right]. \quad (\text{B.13})$$

Third and finally, we wish to express the acceleration in terms of the original Lagrangian coordinates; swapping back can be achieved by evaluating the last equation at the position  $\mathbf{Q} = \mathbf{q} + (\Delta a/2)\nabla_{\mathbf{q}}\varphi^{\text{ini}} + h.o.t.$ , which after straightforward calculations leads to our final result of this appendix,

$$\boxed{\mathbf{A}(\mathbf{q}, \delta a = 0) = -\frac{\Delta a}{2}\nabla_{\mathbf{q}}\varphi^{\text{ini}}(\mathbf{q}) - \left(\frac{\Delta a}{2}\right)^2 \nabla_{\mathbf{q}}^{-1}\mu_2.} \quad (\text{B.14})$$

In deriving this result, the following identity is useful:  $\varphi_{,l}^{\text{ini}}\nabla_{\mathbf{q}}\varphi_{,l}^{\text{ini}} = [1/2]\nabla_{\mathbf{q}}^{-1}(\varphi_{,l}^{\text{ini}}\varphi_{,l}^{\text{ini}})_{,mm}$ . Evidently, eq. (B.14) agrees with (4.3) in the limiting case of an EdS universe, although the respective derivations are quite distinct: In the main text, we performed the acceleration calculation in a completely Lagrangian fashion, while here we have determined it using a semi-Lagrangian approach that relies on swapping between Lagrangian and Eulerian steps in the derivation.

## References

- [1] F. Bernardeau, S. Colombi, E. Gaztanaga and R. Scoccimarro, *Large scale structure of the universe and cosmological perturbation theory*, *Phys. Rep.* **367** (2002) 1 [[astro-ph/0112551](#)].
- [2] S. Dodelson and F. Schmidt, *Modern Cosmology*, Academic Press, second edition ed. (2020), [10.1016/C2017-0-01943-2](#).
- [3] W. Hu and S. Dodelson, *Cosmic Microwave Background Anisotropies*, *Ann. Rev. Astron. Astrophys.* **40** (2002) 171 [[astro-ph/0110414](#)].
- [4] WMAP collaboration, *Nine-Year Wilkinson Microwave Anisotropy Probe (WMAP) Observations: Cosmological Parameter Results*, *Astrophys. J. Suppl.* **208** (2013) 19 [[1212.5226](#)].
- [5] PLANCK collaboration, *Planck 2018 results. VI. Cosmological parameters*, *Astron. Astrophys.* **641** (2020) A6 [[1807.06209](#)].
- [6] F. Beutler, C. Blake, M. Colless, D.H. Jones, L. Staveley-Smith, L. Campbell et al., *The 6dF Galaxy Survey: Baryon Acoustic Oscillations and the Local Hubble Constant*, *Mon. Not. Roy. Astron. Soc.* **416** (2011) 3017 [[1106.3366](#)].
- [7] C. Blake et al., *The WiggleZ Dark Energy Survey: mapping the distance-redshift relation with baryon acoustic oscillations*, *Mon. Not. Roy. Astron. Soc.* **418** (2011) 1707 [[1108.2635](#)].
- [8] Z. Slepian et al., *Constraining the baryon–dark matter relative velocity with the large-scale three-point correlation function of the SDSS BOSS DR12 CMASS galaxies*, *Mon. Not. Roy. Astron. Soc.* **474** (2018) 2109 [[1607.06098](#)].
- [9] R.A.C. Croft, D.H. Weinberg, N. Katz and L. Hernquist, *Recovery of the power spectrum of mass fluctuations from observations of the Lyman alpha forest*, *Astrophys. J.* **495** (1998) 44 [[astro-ph/9708018](#)].
- [10] F.-S. Kitaura, S. Gallerani and A. Ferrara, *Multiscale inference of matter fields and baryon acoustic oscillations from the Ly $\alpha$  forest*, *Mon. Not. Roy. Astron. Soc.* **420** (2012) 61 [[1011.6233](#)].
- [11] H. Gil-Marín, C. Wagner, L. Verde, C. Porciani and R. Jimenez, *Perturbation theory approach for the power spectrum: from dark matter in real space to massive haloes in redshift space*, *JCAP* **2012** (2012) 029 [[1209.3771](#)].
- [12] E. Di Dio, F. Montanari, R. Durrer and J. Lesgourgues, *Cosmological parameter estimation with large scale structure observations*, *JCAP* **2014** (2014) 042 [[1308.6186](#)].
- [13] M. Simonović, T. Baldauf, M. Zaldarriaga, J.J. Carrasco and J.A. Kollmeier, *Cosmological perturbation theory using the FFTLog: formalism and connection to QFT loop integrals*, *JCAP* **2018** (2018) 030 [[1708.08130](#)].
- [14] S.-F. Chen, Z. Vlah and M. White, *Modeling features in the redshift-space halo power spectrum with perturbation theory*, *JCAP* **2020** (2020) 035 [[2007.00704](#)].
- [15] C. Rampf, *Cosmological Vlasov–Poisson equations for dark matter: Recent developments and connections to selected plasma problems*, *Rev. Mod. Plasma Phys.* **5** (2021) 10 [[2110.06265](#)].
- [16] R.E. Angulo and O. Hahn, *Large-scale dark matter simulations*, *Liv. Rev. Comput. Astrophysics* **8** (2022) 1 [[2112.05165](#)].
- [17] M. Crocce, S. Pueblas and R. Scoccimarro, *Transients from initial conditions in cosmological simulations*, *Mon. Not. Roy. Astron. Soc.* **373** (2006) 369 [[astro-ph/0606505](#)].
- [18] M. Pietroni, *Flowing with time: a new approach to non-linear cosmological perturbations*, *JCAP* **2008** (2008) 036 [[0806.0971](#)].
- [19] T. Matsubara, *Resumming cosmological perturbations via the Lagrangian picture: One-loop results in real space and in redshift space*, *Phys. Rev. D* **77** (2008) 063530 [[0711.2521](#)].

- [20] J. Carlson, B. Reid and M. White, *Convolution Lagrangian perturbation theory for biased tracers*, *Mon. Not. Roy. Astron. Soc.* **429** (2013) 1674 [[1209.0780](#)].
- [21] D. Blas, M. Garny and T. Konstandin, *On the non-linear scale of cosmological perturbation theory*, *JCAP* **2013** (2013) 024 [[1304.1546](#)].
- [22] Z. Vlah, U. Seljak and T. Baldauf, *Lagrangian perturbation theory at one loop order: successes, failures, and improvements*, *Phys. Rev. D* **91** (2015) 023508 [[1410.1617](#)].
- [23] C. Rampf, U. Frisch and O. Hahn, *Eye of the Tyger: early-time resonances and singularities in the inviscid Burgers equation*, *Phys. Rev. Fluids* **7** (2022) 104610 [[2207.12416](#)].
- [24] M. Garny, D. Laxhuber and R. Scoccimarro, *Perturbation theory with dispersion and higher cumulants: Nonlinear regime*, *Phys. Rev. D* **107** (2023) 063540 [[2210.08089](#)].
- [25] T. Buchert, *A class of solutions in Newtonian cosmology and the pancake theory*, *Astron. Astrophys.* **223** (1989) 9.
- [26] F. Moutarde, J.M. Alimi, F.R. Bouchet, R. Pellat and A. Ramani, *Precollapse Scale Invariance in Gravitational Instability*, *Astrophys. J.* **382** (1991) 377.
- [27] F.R. Bouchet, R. Juszkiewicz, S. Colombi and R. Pellat, *Weakly Nonlinear Gravitational Instability for Arbitrary Omega*, *Astrophys. J. Letters* **394** (1992) L5.
- [28] T. Buchert, *Lagrangian theory of gravitational instability of Friedman-Lemaitre cosmologies and the 'Zel'dovich approximation'*, *Mon. Not. Roy. Astron. Soc.* **254** (1992) 729.
- [29] F.R. Bouchet, S. Colombi, E. Hivon and R. Juszkiewicz, *Perturbative Lagrangian approach to gravitational instability.*, *Astron. Astrophys.* **296** (1995) 575 [[astro-ph/9406013](#)].
- [30] J. Ehlers and T. Buchert, *Newtonian Cosmology in Lagrangian Formulation: Foundations and Perturbation Theory*, *Gen. Relativ. Gravit.* **29** (1997) 733 [[astro-ph/9609036](#)].
- [31] C. Rampf and T. Buchert, *Lagrangian perturbations and the matter bispectrum I: fourth-order model for non-linear clustering*, *JCAP* **06** (2012) 021 [[1203.4260](#)].
- [32] V. Zheligovsky and U. Frisch, *Time-analyticity of Lagrangian particle trajectories in ideal fluid flow*, *J. Fluid Mech.* **749** (2014) 404 [[1312.6320](#)].
- [33] C. Rampf and U. Frisch, *Shell-crossing in quasi-one-dimensional flow*, *Mon. Not. Roy. Astron. Soc.* **471** (2017) 671 [[1705.08456](#)].
- [34] S. Saga, A. Taruya and S. Colombi, *Lagrangian cosmological perturbation theory at shell-crossing*, *Phys. Rev. Lett.* **121** (2018) 241302 [[1805.08787](#)].
- [35] C. Rampf and O. Hahn, *Shell-crossing in a  $\Lambda$ CDM Universe*, *Mon. Not. Roy. Astron. Soc.* **501** (2021) L71 [[2010.12584](#)].
- [36] C. Rampf, S. Saga, A. Taruya and S. Colombi, *Fast and accurate collapse-time predictions for collisionless matter*, *Phys. Rev. D* **108** (2023) 103513 [[2303.12832](#)].
- [37] M. Pietroni, *Structure formation beyond shell-crossing: nonperturbative expansions and late-time attractors*, *JCAP* **2018** (2018) 028 [[1804.09140](#)].
- [38] C. Rampf, U. Frisch and O. Hahn, *Unveiling the singular dynamics in the cosmic large-scale structure*, *Mon. Not. Roy. Astron. Soc.* **505** (2021) L90.
- [39] S. Colombi, *Vlasov–Poisson in 1D for initially cold systems: post-collapse Lagrangian perturbation theory*, *Mon. Not. Roy. Astron. Soc.* **446** (2015) 2902 [[1411.4165](#)].
- [40] A. Taruya and S. Colombi, *Post-collapse perturbation theory in 1D cosmology – beyond shell-crossing*, *Mon. Not. Roy. Astron. Soc.* **470** (2017) 4858 [[1701.09088](#)].
- [41] S. Saga, S. Colombi and A. Taruya, *The gravitational force field of proto-pancakes*, *Astron. Astrophys.* **678** (2023) A168 [[2305.13354](#)].



- [42] D. Baumann, A. Nicolis, L. Senatore and M. Zaldarriaga, *Cosmological Non-Linearities as an Effective Fluid*, *JCAP* **07** (2012) 051 [[1004.2488](#)].
- [43] M. Pietroni, G. Mangano, N. Saviano and M. Viel, *Coarse-Grained Cosmological Perturbation Theory*, *JCAP* **01** (2012) 019 [[1108.5203](#)].
- [44] J.J.M. Carrasco, M.P. Hertzberg and L. Senatore, *The Effective Field Theory of Cosmological Large Scale Structures*, *JHEP* **09** (2012) 082 [[1206.2926](#)].
- [45] G. Cabass, M.M. Ivanov, M. Lewandowski, M. Mirbabayi and M. Simonović, *Snowmass white paper: Effective field theories in cosmology*, *Phys. Dark Univ.* **40** (2023) 101193 [[2203.08232](#)].
- [46] M.M. Ivanov, *Effective Quantum Gravity*, in *Handbook of Quantum Gravity*, Springer Nature (2023), DOI [[2212.08488](#)].
- [47] V. Desjacques, D. Jeong and F. Schmidt, *Large-Scale Galaxy Bias*, *Phys. Rep.* **733** (2018) 1 [[1611.09787](#)].
- [48] F. Schmidt, F. Elsner, J. Jasche, N.M. Nguyen and G. Lavaux, *A rigorous EFT-based forward model for large-scale structure*, *JCAP* **01** (2019) 042 [[1808.02002](#)].
- [49] F. Schmidt, *Sigma-Eight at the Percent Level: The EFT Likelihood in Real Space*, *JCAP* **04** (2021) 032 [[2009.14176](#)].
- [50] A. Andrews, J. Jasche, G. Lavaux and F. Schmidt, *Bayesian field-level inference of primordial non-Gaussianity using next-generation galaxy surveys*, *Mon. Not. Roy. Astron. Soc.* **520** (2023) 5746 [[2203.08838](#)].
- [51] A. Kostić, N.-M. Nguyen, F. Schmidt and M. Reinecke, *Consistency tests of field level inference with the EFT likelihood*, *JCAP* **07** (2023) 063 [[2212.07875](#)].
- [52] B. Tucci and F. Schmidt, *EFTofLSS meets simulation-based inference:  $\sigma_8$  from biased tracers*, *JCAP* **05** (2024) 063 [[2310.03741](#)].
- [53] N.-M. Nguyen, F. Schmidt, B. Tucci, M. Reinecke and A. Kostić, *How much information can be extracted from galaxy clustering at the field level?*, *arXiv e-prints* (2024) [[2403.03220](#)].
- [54] LSST collaboration, *LSST: from Science Drivers to Reference Design and Anticipated Data Products*, *Astrophys. J.* **873** (2019) 111 [[0805.2366](#)].
- [55] G.D. Racca et al., *The Euclid mission design*, *Proc. SPIE Int. Soc. Opt. Eng.* **9904** (2016) 00 [[1610.05508](#)].
- [56] A. Weltman et al., *Fundamental physics with the Square Kilometre Array*, *Publ. Astron. Soc. Austral.* **37** (2020) e002 [[1810.02680](#)].
- [57] XRISM Science Team, *Science with the X-ray Imaging and Spectroscopy Mission (XRISM)*, *arXiv e-prints* (2020) [[2003.04962](#)].
- [58] T. Eifler, H. Miyatake, E. Krause, C. Heinrich, V. Miranda, C. Hirata et al., *Cosmology with the Roman Space Telescope - multiprobe strategies*, *Mon. Not. Roy. Astron. Soc.* **507** (2021) 1746 [[2004.05271](#)].
- [59] S. Habib et al., *HACC: Simulating Sky Surveys on State-of-the-Art Supercomputing Architectures*, *New Astron.* **42** (2016) 49 [[1410.2805](#)].
- [60] D. Potter, J. Stadel and R. Teyssier, *PKDGRAV3: beyond trillion particle cosmological simulations for the next era of galaxy surveys*, *Comput. Astrophys. Cosmol.* **4** (2017) 2 [[1609.08621](#)].
- [61] N.A. Maksimova, L.H. Garrison, D.J. Eisenstein, B. Hadzhiyska, S. Bose and T.P. Satterthwaite, *AbacusSummit: a massive set of high-accuracy, high-resolution N-body simulations*, *Mon. Not. Roy. Astron. Soc.* **508** (2021) 4017 [[2110.11398](#)].
- [62] T. Ishiyama et al., *The Uchuu simulations: Data Release 1 and dark matter halo concentrations*, *Mon. Not. Roy. Astron. Soc.* **506** (2021) 4210 [[2007.14720](#)].

- [63] F. Villaescusa-Navarro et al., *The Quijote simulations*, *Astrophys. J. Suppl.* **250** (2020) 2 [1909.05273].
- [64] CAMELS collaboration, *The CAMELS project: Cosmology and Astrophysics with Machine Learning Simulations*, *Astrophys. J.* **915** (2021) 71 [2010.00619].
- [65] C. Modi, F. Lanusse and U. Seljak, *FlowPM: Distributed TensorFlow implementation of the FastPM cosmological N-body solver*, *Astron. and Comput.* **37** (2021) 100505 [2010.11847].
- [66] Y. Li, C. Modi, D. Jamieson, Y. Zhang, L. Lu, Y. Feng et al., *Differentiable Cosmological Simulation with the Adjoint Method*, *Astrophys. J. Suppl.* **270** (2024) 36 [2211.09815].
- [67] J. Zeghal, F. Lanusse, A. Boucaud, B. Remy and E. Aubourg, *Neural Posterior Estimation with Differentiable Simulator*, in *Machine Learning for Astrophysics*, p. 52, July, 2022 [2207.05636].
- [68] S. Tassev, M. Zaldarriaga and D.J. Eisenstein, *Solving large scale structure in ten easy steps with COLA*, *JCAP* **2013** (2013) 036 [1301.0322].
- [69] C. Howlett, M. Manera and W.J. Percival, *L-PICOLA: A parallel code for fast dark matter simulation*, *Astron. Comput.* **12** (2015) 109 [1506.03737].
- [70] Y. Feng, M.-Y. Chu, U. Seljak and P. McDonald, *FASTPM: a new scheme for fast simulations of dark matter and haloes*, *Mon. Not. Roy. Astron. Soc.* **463** (2016) 2273 [1603.00476].
- [71] A.E. Bayer, A. Banerjee and Y. Feng, *A fast particle-mesh simulation of non-linear cosmological structure formation with massive neutrinos*, *JCAP* **2021** (2021) 016 [2007.13394].
- [72] F. List and O. Hahn, *Perturbation-theory informed integrators for cosmological simulations*, *J. Comput. Phys.* **513** (2024) 113201 [2301.09655].
- [73] F. List, O. Hahn and C. Rampf, *Starting Cosmological Simulations from the Big Bang*, *Phys. Rev. Lett.* **132** (2024) 131003 [2309.10865].
- [74] R. Scoccimarro and R.K. Sheth, *PTHalos: A Fast Method for Generating Mock Galaxy Distributions*, *Mon. Not. Roy. Astron. Soc.* **329** (2002) 629 [astro-ph/0106120].
- [75] N. Chartier, B. Wandelt, Y. Akrami and F. Villaescusa-Navarro, *CARPool: fast, accurate computation of large-scale structure statistics by pairing costly and cheap cosmological simulations*, *Mon. Not. Roy. Astron. Soc.* **503** (2021) 1897 [2009.08970].
- [76] C. Partmann, C. Fidler, C. Rampf and O. Hahn, *Fast simulations of cosmic large-scale structure with massive neutrinos*, *JCAP* **09** (2020) 018 [2003.07387].
- [77] G. Aricò, R.E. Angulo and M. Zennaro, *Accelerating Large-Scale-Structure data analyses by emulating Boltzmann solvers and Lagrangian Perturbation Theory*, *Open Research Europe* **1** (2022) [2104.14568].
- [78] N. Kokron, J. DeRose, S.-F. Chen, M. White and R.H. Wechsler, *The cosmology dependence of galaxy clustering and lensing from a hybrid N-body-perturbation theory model*, *Mon. Not. Roy. Astron. Soc.* **505** (2021) 1422 [2101.11014].
- [79] N. Chartier and B.D. Wandelt, *CARPool covariance: fast, unbiased covariance estimation for large-scale structure observables*, *Mon. Not. Roy. Astron. Soc.* **509** (2021) 2220 [2106.11718].
- [80] F. Schmidt, *An n-th order Lagrangian Forward Model for Large-Scale Structure*, *JCAP* **04** (2021) 033 [2012.09837].
- [81] T. Matsubara, *On Second-Order Perturbation Theories of Gravitational Instability in Friedmann-Lemaître Models*, *Prog. Theor. Phys.* **94** (1995) 1151 [astro-ph/9510137].
- [82] Y. Brenier, U. Frisch, M. Hénon, G. Loeper, S. Matarrese, R. Mohayaee et al., *Reconstruction of the early Universe as a convex optimization problem*, *Mon. Not. Roy. Astron. Soc.* **346** (2003) 501 [astro-ph/0304214].

- [83] M. Michaux, O. Hahn, C. Rampf and R.E. Angulo, *Accurate initial conditions for cosmological N-body simulations: Minimizing truncation and discreteness errors*, *Mon. Not. Roy. Astron. Soc.* **500** (2020) 663 [2008.09588].
- [84] T. Buchert and J. Ehlers, *Lagrangian theory of gravitational instability of Friedman-Lemaitre cosmologies – second-order approach: an improved model for non-linear clustering*, *Mon. Not. Roy. Astron. Soc.* **264** (1993) 375.
- [85] T. Buchert, *Lagrangian Theory of Gravitational Instability of Friedman-Lemaitre Cosmologies - a Generic Third-Order Model for Nonlinear Clustering*, *Mon. Not. Roy. Astron. Soc.* **267** (1994) 811 [astro-ph/9309055].
- [86] K. Dolag, S. Borgani, S. Schindler, A. Diaferio and A.M. Bykov, *Simulation Techniques for Cosmological Simulations*, *Space Sci. Rev.* **134** (2008) 229 [0801.1023].
- [87] M. Vogelsberger, F. Marinacci, P. Torrey and E. Puchwein, *Cosmological simulations of galaxy formation*, *Nat. Rev. Phys.* **2** (2020) 42 [1909.07976].
- [88] B. Marcos, T. Baertschiger, M. Joyce, A. Gabrielli and F. Sylos Labini, *Linear perturbative theory of the discrete cosmological N-body problem*, *Phys. Rev. D* **73** (2006) 103507 [astro-ph/0601479].
- [89] L.H. Garrison, D.J. Eisenstein, D. Ferrer, M.V. Metchnik and P.A. Pinto, *Improving initial conditions for cosmological N-body simulations*, *Mon. Not. Roy. Astron. Soc.* **461** (2016) 4125 [1605.02333].
- [90] V. Springel, R. Pakmor, O. Zier and M. Reinecke, *Simulating cosmic structure formation with the GADGET-4 code*, *Mon. Not. Roy. Astron. Soc.* **506** (2021) 2871 [2010.03567].
- [91] D. Potter, J. Stadel and R. Teyssier, *PKDGRAV3: beyond trillion particle cosmological simulations for the next era of galaxy surveys*, *Comput. Astrophys. Cosm.* **4** (2017) 2 [1609.08621].
- [92] R. Teyssier, *Cosmological hydrodynamics with adaptive mesh refinement. A new high resolution code called RAMSES*, *Astron. Astrophys.* **385** (2002) 337 [astro-ph/0111367].
- [93] M. Schaller, J. Borrow, P.W. Draper, M. Ivkovic, S. McAlpine, B. Vandenbroucke et al., *SWIFT: A modern highly-parallel gravity and smoothed particle hydrodynamics solver for astrophysical and cosmological applications*, *Mon. Not. Roy. Astron. Soc.* (2024) [2305.13380].
- [94] A.A. Klypin and S.F. Shandarin, *Three-dimensional numerical model of the formation of large-scale structure in the Universe.*, *Mon. Not. Roy. Astron. Soc.* **204** (1983) 891.
- [95] G. Efstathiou, M. Davis, S.D.M. White and C.S. Frenk, *Numerical techniques for large cosmological N-body simulations*, *Astrophys. J. Suppl.* **57** (1985) 241.
- [96] T. Quinn, N. Katz, J. Stadel and G. Lake, *Time stepping N-body simulations*, *arXiv e-prints* (1997) astro [astro-ph/9710043].
- [97] C. Rampf, S.O. Schobesberger and O. Hahn, *Analytical growth functions for cosmic structures in a  $\Lambda$ CDM Universe*, *Mon. Not. Roy. Astron. Soc.* **516** (2022) 2840 [2205.11347].
- [98] N. Kokron, J. DeRose, S.-F. Chen, M. White and R.H. Wechsler, *Priors on red galaxy stochasticity from hybrid effective field theory*, *Mon. Not. Roy. Astron. Soc.* **514** (2022) 2198 [2112.00012].
- [99] A. Izard, M. Crocce and P. Fosalba, *ICE-COLA: Towards fast and accurate synthetic galaxy catalogues optimizing a quasi N-body method*, *Mon. Not. Roy. Astron. Soc.* **459** (2016) 2327 [1509.04685].
- [100] J. Koda, C. Blake, F. Beutler, E. Kazin and F. Marin, *Fast and accurate mock catalogue generation for low-mass galaxies*, *Mon. Not. Roy. Astron. Soc.* **459** (2016) 2118 [1507.05329].
- [101] O. Hahn and R.E. Angulo, *An adaptively refined phase-space element method for cosmological simulations and collisionless dynamics*, *Mon. Not. Roy. Astron. Soc.* **455** (2016) 1115 [1501.01959].
- [102] J. Stücker, O. Hahn, R.E. Angulo and S.D.M. White, *Simulating the complexity of the dark matter sheet I: numerical algorithms*, *Mon. Not. Roy. Astron. Soc.* **495** (2020) 4943 [1909.00008].

- [103] A.K. Chaniotis and D. Poulidakos, *High order interpolation and differentiation using B-splines*, *J. Comput. Phys.* **197** (2004) 253.
- [104] R.W. Hockney and J.W. Eastwood, *Computer simulation using particles*, Routledge and CRC Press, Boca Raton, FL, USA (1988), [10.1201/9780367806934](https://doi.org/10.1201/9780367806934).
- [105] S.A. Orszag, *On the Elimination of Aliasing in Finite-Difference Schemes by Filtering High-Wavenumber Components*, *J. Atmos. Sci.* **28** (1971) 1074.
- [106] A. Taruya, T. Nishimichi and D. Jeong, *Grid-based calculation for perturbation theory of large-scale structure*, *Phys. Rev. D* **98** (2018) 103532 [[1807.04215](https://arxiv.org/abs/1807.04215)].
- [107] A. Taruya, T. Nishimichi and D. Jeong, *Grid-based calculations of redshift-space matter fluctuations from perturbation theory: UV sensitivity and convergence at the field level*, *Phys. Rev. D* **105** (2022) 103507 [[2109.06734](https://arxiv.org/abs/2109.06734)].
- [108] C. Rampf and Y.Y.Y. Wong, *Lagrangian perturbations and the matter bispectrum II: the resummed one-loop correction to the matter bispectrum*, *JCAP* **06** (2012) 018 [[1203.4261](https://arxiv.org/abs/1203.4261)].
- [109] M. Fasiello, T. Fujita and Z. Vlah, *Perturbation theory of large scale structure in the  $\Lambda$ CDM Universe: Exact time evolution and the two-loop power spectrum*, *Phys. Rev. D* **106** (2022) 123504 [[2205.10026](https://arxiv.org/abs/2205.10026)].
- [110] T. Baldauf, E. Schaan and M. Zaldarriaga, *On the reach of perturbative descriptions for dark matter displacement fields*, *JCAP* **03** (2016) 017 [[1505.07098](https://arxiv.org/abs/1505.07098)].
- [111] D.J. Bartlett, M. Chiarenza, L. Doerer and F. Leclercq, *COMoving Computer Acceleration (COCA): N-body simulations in an emulated frame of reference*, *arXiv e-prints* (2024) [[2409.02154](https://arxiv.org/abs/2409.02154)].
- [112] D.K. Ramanah, G. Lavaux, J. Jasche and B.D. Wandelt, *Cosmological inference from Bayesian forward modelling of deep galaxy redshift surveys*, *Astron. Astrophys.* **621** (2019) A69 [[1808.07496](https://arxiv.org/abs/1808.07496)].
- [113] S. He, Y. Li, Y. Feng, S. Ho, S. Ravanbakhsh, W. Chen et al., *Learning to Predict the Cosmological Structure Formation*, *Proc. Nat. Acad. Sci.* **116** (2019) 13825 [[1811.06533](https://arxiv.org/abs/1811.06533)].
- [114] F. Elsner, F. Schmidt, J. Jasche, G. Lavaux and N.-M. Nguyen, *Cosmology inference from a biased density field using the EFT-based likelihood*, *JCAP* **01** (2020) 029 [[1906.07143](https://arxiv.org/abs/1906.07143)].
- [115] S.S. Boruah and E. Rozo, *Map-based cosmology inference with weak lensing – information content and its dependence on the parameter space*, *Mon. Not. Roy. Astron. Soc.* **527** (2023) L162 [[2307.00070](https://arxiv.org/abs/2307.00070)].
- [116] W. Elbers, C.S. Frenk, A. Jenkins, B. Li and S. Pascoli, *Higher order initial conditions with massive neutrinos*, *Mon. Not. Roy. Astron. Soc.* **516** (2022) 3821 [[2202.00670](https://arxiv.org/abs/2202.00670)].
- [117] J.Z. Chen, A. Upadhye and Y.Y.Y. Wong, *One line to run them all: SuperEasy massive neutrino linear response in N-body simulations*, *JCAP* **04** (2021) 078 [[2011.12504](https://arxiv.org/abs/2011.12504)].
- [118] P. Heuschling, C. Partmann and C. Fidler, *A minimal model for massive neutrinos in Newtonian N-body simulations*, *JCAP* **09** (2022) 068 [[2201.13186](https://arxiv.org/abs/2201.13186)].
- [119] O. Hahn, F. List and N. Porqueres, *DISCO-DJ I: a differentiable Einstein-Boltzmann solver for cosmology*, *JCAP* **06** (2024) 063 [[2311.03291](https://arxiv.org/abs/2311.03291)].
- [120] V. Springel, *The cosmological simulation code GADGET-2*, *Mon. Not. Roy. Astron. Soc.* **364** (2005) 1105 [[astro-ph/0505010](https://arxiv.org/abs/astro-ph/0505010)].
- [121] M. Vermeeren, A. Bravetti and M. Seri, *Contact variational integrators*, *J. Phys. A: Math. Theor.* **52** (2019) 1 [[1902.00436](https://arxiv.org/abs/1902.00436)].
- [122] O. Podvigina, V. Zheligovsky and U. Frisch, *The Cauchy-Lagrangian method for numerical analysis of Euler flow*, *J. Comput. Phys.* **306** (2016) 320 [[1504.05030](https://arxiv.org/abs/1504.05030)].